Point-to-point responses

*We appreciate the reviewers for their valuable and constructive comments, which are very helpful for the improvement of the manuscript. We have revised the manuscript carefully according to the reviewers' comments. We have addressed the reviewers' comments on a point-to-point basis as below for consideration, where the reviewers' comments are cited in **black**, and the responses are in **blue**.*

Referee #1

Xing et al. learned the vertical variations and sources of O_3 and HONO and their precursors on the Tibetan Plateau. The authors found that the contributions of HONO and O_3 to the production rates of OH on the TP are even greater than at lower-altitudes areas. This study will enrich the new understanding of vertical distribution of atmospheric components and explained the strong AOC on the TP. From the point of view of the data and scientific value, I recommend this manuscript being published in ACP after following revisions.

1. Authors should reorganize the abstract. The significance of the research and the most significant scientific findings should be fully presented.
Re: Thanks for your great comments. We have reorganized the abstract as following:
"The Tibetan Plateau (TP) plays a key role in regional environment and global climate change, however, the lack of vertical observation of atmospheric species, such as HONO and O_3, hinders a deeper understanding of the atmospheric chemistry and atmospheric oxidation capacity (AOC) on the TP. In this study, we conducted multi-axis differential optical absorption spectroscopy (MAX-DOAS) measurements at Nam Co, the central TP, to observe the vertical profiles of aerosol, water vapor (H_2O), NO_2, HONO and O_3 from May to July 2019. In addition to NO_2 mainly exhibiting a Gaussian shape with the maximum value appearing at 300-400 m, other four species all showed an exponential shape and decreased with the increase of height. The maximum values of monthly averaged aerosol (0.17 km^{-1}) and O_3 (66.71 ppb) occurred on May, H_2O (3.68×10^{17} molec cm^{-3}) and HONO (0.13 ppb) appeared on July, while NO_2 (0.39 ppb) occurred on June at 200-400 m layer. H_2O, HONO and O_3 all exhibited a multi-peak pattern, and aerosol appeared a bi-peak pattern for their averaged diurnal variations. The averaged vertical profiles of OH production rates from O_3 and HONO all exhibited an exponential shape decreasing with the increase of height with maximum values of 2.61 ppb/h and 0.49 ppb/h at the bottom layer, respectively. The total OH production rate contributed by HONO and O_3 on the TP was obviously larger than that in low-altitude areas. In addition, source analysis for HONO and O_3 at different height layers were conducted. The heterogeneous reaction of NO_2 on wet surfaces was a significant source of HONO. The maximum values of HONO/NO_2 appeared around H_2O being 1.0×10^{17} molec cm^{-3} and aerosol being lager 0.15 km^{-1} under 1.0 km, and the maximum values usually accompanied with H_2O being $1.0-2.0\times10^{17}$ molec cm^{-3} and aerosol being lager 0.02 km^{-1} at 1.0-2.0 km. O_3 was potentially sourced from south Asian

subcontinent and Himalayas through long-range transport. Our results enrich the new understanding of vertical distribution of atmospheric components and explained the strong AOC on the TP."

2.The description of the retrieval algorithm and the corresponding uncertainty analysis of vertical profiles is missing. The authors could even put them in the supplementary materials.

Re: Thanks for your great comments.

● *Vertical profile retrieval algorithm*

The atmospheric vertical profile (aerosol, H_2O, NO_2, HONO, and O_3) retrieval algorithm from MAX-DOAS measurements was developed based on the optimal estimation method and used radiative transfer model as the forward model (Lin et al., 2020; Liu et al., 2022; Ji et al., 2023; Xing et al., 2023). The maximum a posteriori state vector x is determined by minimizing the following cost function χ^2.

$$\chi^2 = \left(y - F\left(x,b\right)\right)^T S_\varepsilon^{-1}\left(y - F\left(x,b\right)\right) + \left(x - x_a\right)^T S_a^{-1}\left(x - x_a\right)$$

Here, $F\left(x,b\right)$ is the forward model, which describes the measured DSCDs y as a function of the retrieval state vector x (i.e., aerosol and trace gas vertical profiles) and the meteorological parameters b (e.g., atmospheric pressure and temperature profiles); x_a denotes the a priori vector that serves as an additional constraint; S_ε and S_a are the covariance matrices of y and x_a, respectively. The retrieval of vertical profiles of aerosols and trace gases were classified into two steps. Firstly, we retrieved vertical aerosol profiles based on a series of retrieved O_4 DSCDs at different elevation angles. Secondly, the retrieved aerosol profiles were utilized as the input parameters to the radiative transfer model to retrieve H_2O, NO_2 and HONO profiles. Considering the strong O_3 absorption in the stratosphere, the retrieval of the tropospheric O_3 profile must remove the influence of stratospheric O_3. In this study, daily stratospheric O_3 profiles from TROPOMI measurements were included in the radiative transfer model simulation for tropospheric O_3 profile retrieval to account for the influence of stratospheric O_3 absorption on the retrieval.

● *Error analysis*

The error sources can be divided into four different types: smoothing error, noise error, forward model error, and model parameter error (Rodgers, 2004). However, in terms of this classification, some errors are difficult to be calculated or estimated. For example, the forward model error, which is caused by an imperfect representation of the physics of the system, is hard to be quantified due to the difficulty of acquiring an improved forward model. Given calculation convenience and contributing ratios of different errors in total error budget, we mainly took into account following error sources, which were smoothing and noise errors, algorithm error, cross section error, and uncertainty related to the aerosol retrieval (only for trace gas). In this study, we estimated the

contribution of different error sources to the AOD and VCDs of trace gases, and near-surface (0–200 m) trace gases' concentrations and aerosol extinction coefficients (AECs), respectively. The detailed demonstrations and estimation methods are displayed below, and the corresponding varies errors are summarized in Table R1.

a. Smoothing errors arise from the limited vertical resolution of profile retrieval. Noise errors denote the noise in the spectra (i.e., the error of DOAS fits). Considering the error of the retrieved state vector equaling the sum of these two independent errors, we calculated the sum of smoothing and noise errors on near-surface concentrations and column densities, which were 13 and 5 % for aerosols, 13 and 36 % for H_2O, 12 and 14 % for NO_2, 18 and 21 % for HONO, and 12 and 32 % for O_3, respectively.

b. Algorithm error is denoted by the differences between the measured and simulated DSCDs. This error contains forward model error from an imperfect approximation of forward function, parameter error of forward model, and other errors, such as detector noise (Rodgers, 2004). Algorithm error is a function of the viewing angle, and it is difficult to assign this error to each altitude. Thus, this error on the near-surface values and column densities is estimated through calculating the average relative differences between the measured and simulated DSCDs at the minimum and maximum elevation angle (except 90°), respectively (Wagner et al., 2004). In this study, we estimated these errors on the near-surface values and the column densities at 4 and 8 % for aerosols, 3 and 11 % for NO_2, and 20 and 20 % for HONO referring to Wang et al. (2017, 2020), 1 and 8 % for H_2O referring to Lin et al. (2020), and 6 and 10 % for O_3 referring to Ji et al. (2023), respectively.

c. Cross section error arises from the uncertainty in the cross section. According to Thalman and Volkamer, (2013), Lin et al. (2020), Vandaele et al. (1998), Stutz et al. (2000), and Serdyuchenko et al. (2014), we adopted 4, 3, 3, 5, and 2 % for O_4 (aerosols), H_2O, NO_2, HONO and O_3, respectively.

d. The profile retrieval error for trace gases is sourced from the uncertainty of aerosol extinction profile retrieval and propagated to trace gas profile. This error could be roughly estimated based on a linear propagation of the total error budgets of the aerosol retrievals. The errors of the learned four trace gases were roughly estimated at 14 % for VCDs and 10 % for near-surface concentrations, respectively.

The total uncertainty was the sum of all above errors in the Gaussian error propagation, and the error results were listed in Table R1. We found that the smoothing and noise errors played a dominant role in the total uncertainties of aerosol and trace gases. Moreover, improving the accuracy and temperature gradient of the absorption cross section is another important means to reduce the uncertainty of the vertical profiles in the future, especially for O_3.

Table R1. Error budget estimation (in %) of the retrieved near-surface (0–200 m) concentrations of trace gases and AECs, and AOD and VCDs.

		Error sources				Total
		Smoothing and noise errors	Algorithm error	Cross section error	Related to the aerosol retrieval (only for trace gases)	
Near-surface	aerosol	13	4	4	-	14
	H_2O	13	1	3	14	19

	NO$_2$	12	3	3	14	18
	HONO	18	20	5	14	29
	O$_3$	12	6	2	14	19
VCD or AOD	AOD	5	8	4	-	10
	H$_2$O	36	8	3	10	38
	NO$_2$	14	11	3	10	20
	HONO	21	20	5	10	31
	O$_3$	32	10	2	10	35

3.Section 2.1 emphasized HCHO, which seems to be irrelevant to this study. I suggest the authors to modificate Figure S1 to narrow the area and focus on the area around Nam Co.

Re: Thanks for your great comments. We have modified Figure S1 as following. The HCHO was removed and the study area was narrowed down.
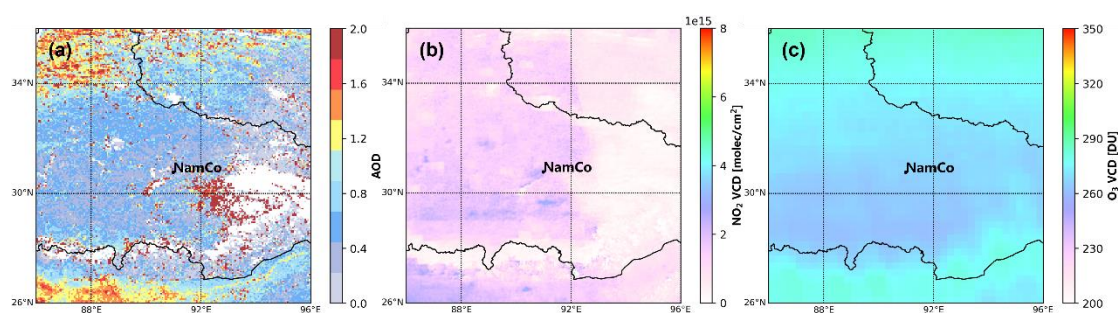

Figure R2 (S1). Averaged spatial distributions of (a) AOD monitored by Himawari-8, (b) NO$_2$ VCDs monitored by TROPOMI, (and c) O$_3$ total VCDs monitored by OMI from May to July 2019 in Nam Co.

4.The authors concluded "high concentration NO$_2$ should be attributed to the transport process from the NOx produced by ice and snow on the top of Mt. Tanggula". Can you give adequate data and literature support?

Re: Thanks for your great comments. Firstly, we added two important literatures as following to support this conclusion.

(1) Fisher F N. Extinction of UV-visible radiation in wet midlatitude (maritime) snow: Implications for increased NO$_x$ emission. Journal of Geophysical Research, 110, D21301, doi:10.1029/2005JD005963, 2005. *The main point was that snow cover in mid-latitude mountainous areas contributed significantly to NO$_x$ emissions.*

(2) Lin W, Wang F, Ye C, Zhu T. Observation of strong NO$_x$ release over Qiyi Glacier, China. The Cryosphere, doi.org/10.5194/tc-2021-32, 2021. *The main point was that high NO$_x$ production was due to photochemical reactions on the snow surface of the Tibetan Plateau.*

Secondly, we also did WPSCF analysis, and the WPSCF passing through Mt. Tanggula showed high values at 300-400 m layer, especially at 400 m (> 0.3). It indicated that the important contribution to NO$_x$ from ice and snow on the top of Mt. Tanggula under strong ultraviolet radiation.
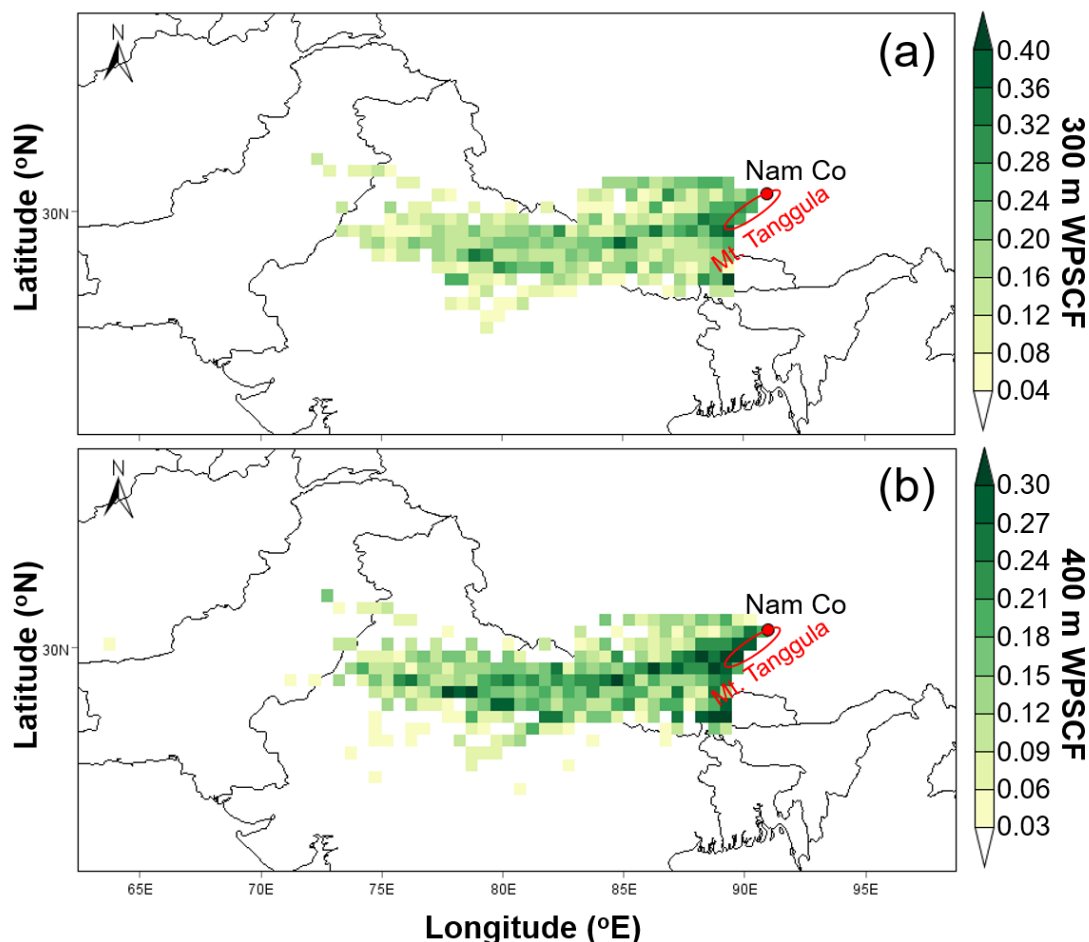
Figure R3 (S3). Spatial distributions of 24-h WPSCF values for NO_2 at (a) 300 m, and (b) 400 m height layers from 01 May to 09 July 2019 over CAS (NAMORS).

5. P6 L194-197, "Moreover, the large-scaled spatial distributions of AOD, O_3, NO_2 and HCHO over CAS (NAMORS) were monitored by Himawari-8 (Bessho et al., 2016), OMI (Veefkind et al., 2004) and TROPOMI (Griffin et al., 2018; Su et al., 2020), respectively."

Re: Thanks for your great comments. Referred to comment 3, we removed HCHO, and rewritten this sentence as "Moreover, the large-scaled spatial distributions of AOD, O_3 and NO_2 over CAS (NAMORS) were monitored by Himawari-8 (Bessho et al., 2016), OMI (Veefkind et al., 2004) and TROPOMI (Griffin et al., 2018; Su et al., 2020), respectively."

6. P6L202, increases > increased

Re: Thanks for your great comments. We have rewritten this sentence as "Subsequently, the AOD increases significantly, reaching maximum values during 15:00-17:00 (average of 0.107km-1), which was about 1.408 times the diurnal average value.".

7. P7L212-213, shown > was, and > but

Re: Thanks for your great comments. We have rewritten this sentence as "As shown in

Figure S2, the diurnal variation of PBL in Nam Co from May to July 2019 was lower in the early morning and late afternoon, but higher between 11:00 and 17:00 with the maximum PBL larger than 2.0 km.".

8. P12L390, first > firstly

Re: Thanks for your great comments. We have rewritten this sentence as "This phenomenon of $HONO/NO_2$ firstly increasing and then decreasing with the increasing of water vapor (or relative humidity) was usually found in low-altitude areas in previous studies (Wang et al., 2013; Liu et al., 2019; Xing et al., 2021; Xu et al., 2021).".

References

Fisher F N. Extinction of UV-visible radiation in wet midlatitude (maritime) snow: Implications for increased NO_x emission. Journal of Geophysical Research, 110, D21301, doi:10.1029/2005JD005963, 2005.

Lin W, Wang F, Ye C, Zhu T. Observation of strong NO_x release over Qiyi Glacier, China. The Cryosphere, doi.org/10.5194/tc-2021-32, 2021.

Ji X, Liu C, Wang Y, Hu Q, Lin H, Zhao F, Xing C, Tang G, Zhang J, Wagner T. Ozone profiles without blind area retrieved from MAX-DOAS measurements and comprehensive validation with multi-platform observations. Remote Sensing of Environment, 284, 113339, doi.org/10.1016/j.res.2022.113339, 2023.

Liu C, Xing C, Hu Q, Li Q, Liu H, Hong Q, Tan W, Ji X, Lin H, Lu C, Lin J, Liu H, Wei S, Chen J, Yang K, Wang S, Liu T, Chen Y. Ground-based hyperspectral stereoscopic remote sensing network: A promising strategy to learn coordinated control of O_3 and $PM_{2.5}$ over China. Engineering, 19, 71-83, doi.org/10.1016/j.eng.2021.02.019, 2022.

Lin H, Liu C, Xing C, Hu Q, Hong Q, Liu H, Li Q, Tan W, Ji X, Wang Z, Liu J. Validation of water vapor vertical distributions retrieved from MAX-DOAS over Beijing, China. Remote Sensing, 12, 3193, doi.org/10.3390/rs12193193, 2020.

Xing C, Xu S, Song Y, Liu C, Liu Y, Lu K, Tan W, Zhang C, Hu Q, Wang S, Wu H, Lin H. A new insight into the vertical differences in NO_2 heterogeneous reaction to produce HONO over inland and marginal seas. Atmospheric Chemistry and Physics, 23, 5815-5834, doi.org/10.5194/acp-23-5815-2023, 2023.

Rodgers C D. Inverse methods for atmospheric sounding: theory and practice. Singapore-New Jersey-London-Hong: World Scientific Publishing; 2000.

Wagner T, Dix B, FriedeBurg C V, Frieß U, Sanghavi S, Sinreich R, Platt U. MAX-DOAS O_4 measurements: A new technique to derive information on atmospheric aerosols-Principles and information content. Journal of Geophysical Research: Atmospheres, 109, D22205, doi.org/10.1029/2004jd004904, 2004.

Serdyuchenko A, Gorshelev V, Weber M, Chehade W, Burrows J P. High spectral resolution ozone absorption cross-sections-Part 2: Temperature dependence. Atmospheric Measurement Techniques, 7, 625-636, doi:10.5194/amt-7-625-2014, 2014.

Wang Y, Lampel J, Xie P, Beirle S, Li A, Wu D, Wagner T. Ground-based MAX-DOAS observations of tropospheric aerosols, NO_2, SO_2 and HCHO in Wuxi, China, from 2011 to 2014. Atmospheric Chemistry and Physcis, 17, 2189-2215, doi.org/10.5194/acp-17-2189-2017, 2017.

Wang Y, Apituley A, Bais A, Beirle S, Benavent N, Borovski A, Bruchkouski I, Chan K L, Donner S, Drosoglou T, Finkenzeller H, Friedrich M M, Frieß U, Garcia-Nieto D, Gómez-Martín L, Hendrick F, Hilboll A, Jin J, Johnston P, Koenig T K, Kreher K, Kumar V, Kyuberis A, Lampel J, Liu C, Liu H, Ma J, Polyansky O L, Postylyakov O, Querel R, Saiz-Lopez A, Schmitt S, Tian X, Tirpitz J L, Van Roozendeal M, Volkamer R, Wang Z, Xie P, Xing C, Xu J, Yela M, Zhang C, Wagner T. Inter-comparison of MAX-DOAS measurements of tropospheric HONO slant column densities and vertical

profiles during the CINDI-2 campaign. Atmospheric Measurement Techniques, 13, 5087–5116, doi.org/10.5194/amt-13-5087-2020, 2020.

Thalman R, Volkamer R. Temperature dependent absorption cross-sections of O_2-O_2 collision pairs between 340 and 630 nm and at atmospherically relevant pressure. Physical Chemistry Chemical Physics, 15, 15371-15381, 2013.

Vandaele A C, Hermans C, Simon P C, Carleer M, Colin R, Fally S, Merienne M F, Jenouvrier A, Coquart D. Measurements of the NO_2 absorption cross-section from 42000 cm^{-1} to 10000 cm^{-1} (238–1000nm) at 220K and 294K. Journal of Quantitative Spectroscopy and Radiative Transfer, 59, 171-184, 1998.

Stutz J, Kim E S, Platt U, Bruno P, Perrino C, Febo A. UV-visible absorption cross sections of nitrous acid. Journal of Geophysical Research: Atmospheres, 105, 14585-14592, 2000.

Referee #2

This manuscript describes ground-based MAX-DOAS measurements in Nam Co over the Tibetan Plateau (TP). The measurements are used to obtain vertical distributions of several atmospheric components (aerosol, H_2O, NO_2, HONO and O_3) via spectral analysis and OEM profile retrieval. The data are further used to analyze the temporal and vertical evolutions for these species. The OH production as well as possible daytime HONO and O_3 sources were also discussed during the field campaign. Overall, observing and investigating the vertical profiles of atmospheric components at the background station in the relatively remote and high-altitude region are significant. However, two concerns at least should be clarified in detail before the manuscript is considered to be accepted.

(1) Firstly, the reliabilities of vertical profile of atmospheric components (aerosol, H_2O, NO_2, HONO and O_3) should be validated. Just using the parameter setting scheme of spectral analysis and profile retrieval in previous studies won't do for the specific station over the TP. For example, the HONO spectral structures are almost drowned in the noise in Figure 2d. The sensitivity tests about the parameter setting scheme of spectral analysis and profile retrieval should be presented in detail. In addition, just according to the comparison of surface multi-source data in Section 3.3, it cannot illustrate the reliabilities of vertical profiles. Also, the correlation was weak for HONO (R^2=0.38) with larger deviations in Figure 6b.

Re: Thanks for your great comments.

We added a section of "*2.2.3 Error analysis*" to ensure the reliability of data.

The error sources can be divided into four different types: smoothing error, noise error, forward model error, and model parameter error (Rodgers, 2004). However, in terms of this classification, some errors are difficult to be calculated or estimated. For example, the forward model error, which is caused by an imperfect representation of the physics of the system, is hard to be quantified due to the difficulty of acquiring an improved forward model. Given calculation convenience and contributing ratios of different errors in total error budget, we mainly took into account following error sources, which were smoothing and noise errors, algorithm error, cross section error, and uncertainty related to the aerosol retrieval (only for trace gas). In this study, we estimated the contribution of different error sources to the AOD and VCDs of trace gases, and near-surface (0–200 m) trace gases' concentrations and aerosol extinction coefficients (AECs), respectively. The detailed demonstrations and estimation methods are displayed below, and the corresponding varies errors are summarized in Table R1.

e. Smoothing errors arise from the limited vertical resolution of profile retrieval. Noise errors denote the noise in the spectra (i.e., the error of DOAS fits). Considering the error of the retrieved state vector equaling the sum of these two independent errors, we calculated the sum of smoothing and noise errors on near-surface concentrations and column densities, which were 13 and 5 % for aerosols, 13 and 36 % for H_2O, 12 and 14 % for NO_2, 18 and 21 % for HONO, and 12 and 32 % for O_3, respectively.

f. Algorithm error is denoted by the differences between the measured and simulated DSCDs. This error contains forward model error from an imperfect approximation of forward function, parameter error of forward model, and other errors, such as detector noise (Rodgers, 2004). Algorithm error is a function of the viewing angle, and it is difficult to assign this error to each altitude. Thus, this error on the near-surface values and column densities is estimated through calculating the average relative differences between the measured and simulated DSCDs at the minimum and maximum elevation angle (except 90°), respectively (Wagner et al., 2004). In this study, we estimated these errors on the near-surface values and the column densities at 4 and 8 % for aerosols, 3 and 11 % for NO_2, and 20 and 20 % for HONO referring to Wang et al. (2017, 2020), 1 and 8 % for H_2O referring to Lin et al. (2020), and 6 and 10 % for O_3 referring to Ji et al. (2023), respectively.

g. Cross section error arises from the uncertainty in the cross section. According to Thalman and Volkamer, (2013), Lin et al. (2020), Vandaele et al. (1998), Stutz et al. (2000), and Serdyuchenko et al. (2014), we adopted 4, 3, 3, 5, and 2 % for O_4 (aerosols), H_2O, NO_2, HONO and O_3, respectively.

h. The profile retrieval error for trace gases is sourced from the uncertainty of aerosol extinction profile retrieval and propagated to trace gas profile. This error could be roughly estimated based on a linear propagation of the total error budgets of the aerosol retrievals. The errors of the learned four trace gases were roughly estimated at 14 % for VCDs and 10 % for near-surface concentrations, respectively.

The total uncertainty was the sum of all above errors in the Gaussian error propagation, and the error results were listed in Table R1. We found that the smoothing and noise errors played a dominant role in the total uncertainties of aerosol and trace gases. Moreover, improving the accuracy and temperature gradient of the absorption cross section is another important means to reduce the uncertainty of the vertical profiles in the future, especially for O_3.

Table R1. Error budget estimation (in %) of the retrieved near-surface (0–200 m) concentrations of trace gases and AECs, and AOD and VCDs.

		Error sources				Total
		Smoothing and noise errors	Algorithm error	Cross section error	Related to the aerosol retrieval (only for trace gases)	
Near-surface	aerosol	13	4	4	-	14
	H_2O	13	1	3	14	19
	NO_2	12	3	3	14	18
	HONO	18	20	5	14	29
	O_3	12	6	2	14	19
VCD or AOD	AOD	5	8	4	-	10
	H_2O	36	8	3	10	38
	NO_2	14	11	3	10	20
	HONO	21	20	5	10	31
	O_3	32	10	2	10	35

Certainly, we also did independent validations. However, there was not other vertical observations during our campaign on the TP. Therefore, we did validations between in situ measurements and the bottom layer of MAX-DOAS profiles (Figure R1).
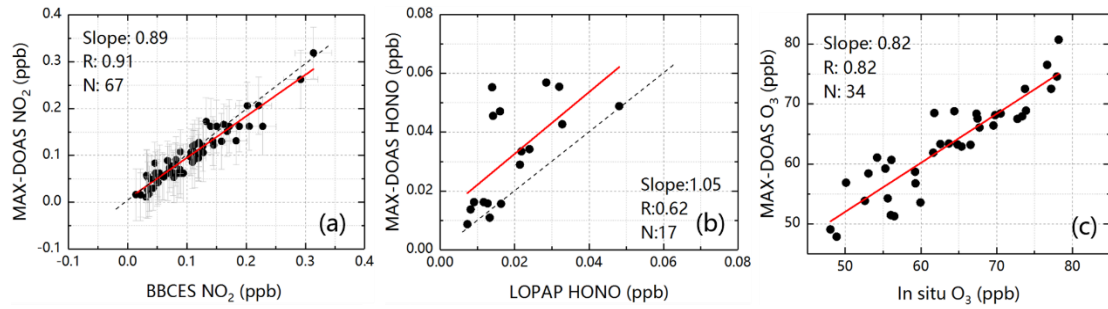
Figure R1. Validations of (a) MAX-DOAS NO_2 vs in situ NO_2, (b) MAX-DOAS HONO vs LOPAP HONO, (c) MAX-DOAS O_3 vs in situ O_3.

Moreover, we did vertical-profile validations in Shanghai and Beijing. As shown in Figure R2, we used Mie lidar to validate MAX-DOAS aerosol vertical profiles, and used balloon-based NO_2 profiles to validate MAX-DOAS NO_2 vertical profiles (Xing et al., 2017). The good agreement indicates the reliability of MAX-DOAS retrieved aerosol and NO_2 profiles.
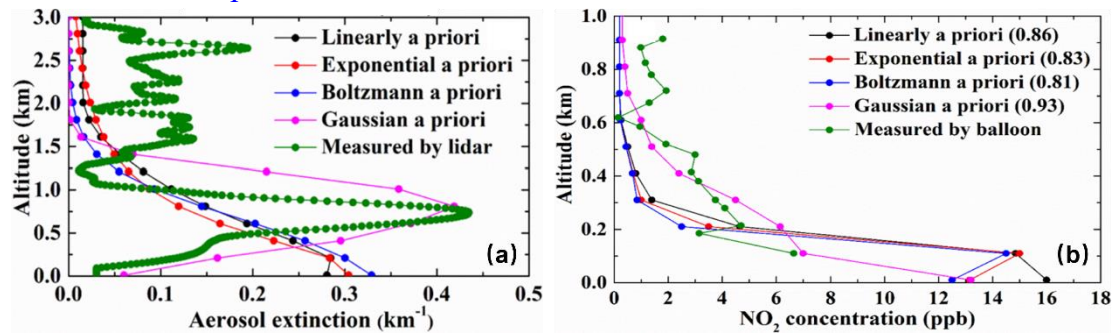

Figure R2. Validations of (a) MAX-DOAS aerosol profile vs lidar aerosol profile, (b) MAX-DOAS NO_2 profile vs balloon-based NO_2 profile.

As shown in Figure R3, the retrieved O_3 profiles were validated with tower-based O_3 profiles in Beijing. The correlation coefficients (R) between them on 2 m, 60 m, 160 m, and 280 m were 0.844, 0.864, 0.883 and 0.902, respectively.
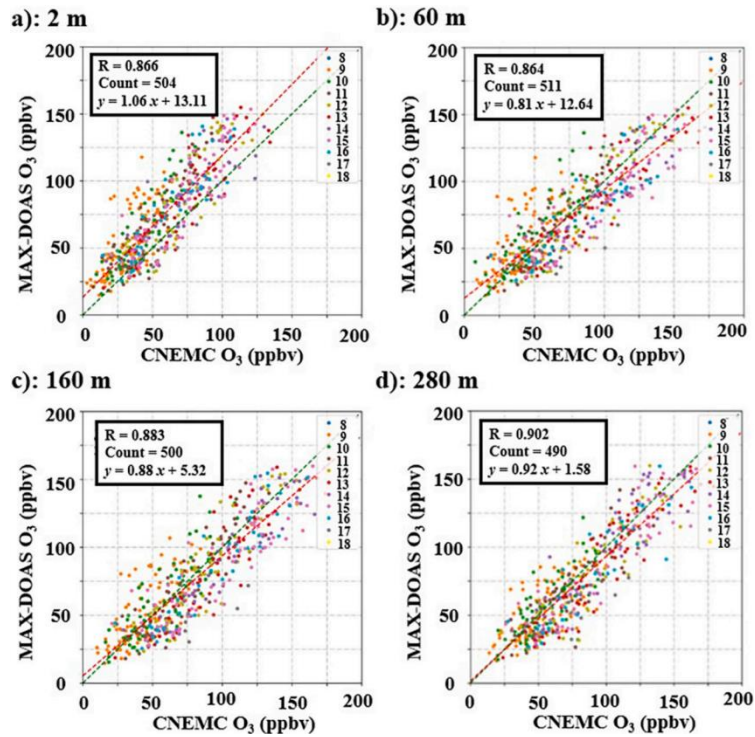
Figure R3. Validations of MAX-DOAS O$_3$ profile vs tower-based O$_3$ profile at four height layers (a) 2 m, (b) 60 m, (c) 160 m, and (d) 280 m.

As shown in Figure R4, we re-selected a representative HONO fitting result. We can be sure that the HONO results used in the manuscript all from well spectra fittings. Considering the effects of low concentration and weak absorption of HONO, and spectral noise, we performed third-order averaging of the spectra during spectral analysis.
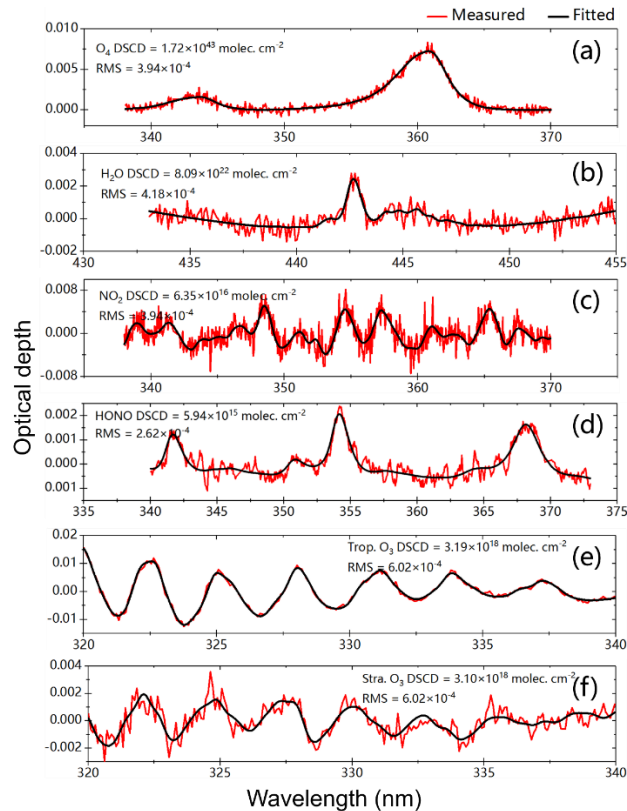
Figure R4. DOAS fit examples of O_4, H_2O, NO_2, HCHO, tropospheric O_3 and stratospheric O_3. The red line and black line represent the measured and fitted results, respectively.

About the weak correlation of HONO (R=0.62) between MAX-DOAS measurements and LOPAP measurements, we make it clear that uncertainties also appear in the LOPAP HONO results during the observation period (Wang et al., 2023). Longer HONO observations on the TP based on more instruments are needed in the future, in order to further analyze the uncertainty of HONO observations among different instruments.

(2) The manuscript tried to analyze the OH production (Section 4.1) from HONO and O_3 at different height layers through vertical observations and TUV calculations. The TUV model is suitable for exploring the photolysis rates, but OH production is determined by complex chemical process involving many atmospheric components. The equations in Line 342 and 343 are simplified for studying OH production. It should present more details on the parameter scheme during simulation by TUV model, and more comparisons of OH production simulated by other models if possible.

Re: Thanks for your great comments.

In this study, we used online TUV model.

https://www2.acom.ucar.edu/modeling/tropospheric-ultraviolet-and-visible-tuv-radiation-model

The main parameters for this model were cloud information, total ozone column, aerosol optical depth (AOD), single scattering albedo (SSA), and Ångström exponents. In this study, we selected clean and cloud free days (Figure R6), the AOD at 361 nm was derived from aerosol extinction profiles measured by MAX-DOAS; the daily total ozone column density was measured by TROPOMI with a value range of 260-280 DU; the single scattering albedo (SSA) was calculated based on the regression analysis of multi-wavelength (361 and 477 nm) O_4 absorptions measured by MAX-DOAS (Xing et al., 2019); fixed Ångström exponents of 0.508, 0.581 and 0.713 were used in May, June and July, respectively, referring to Xia et al. (2011).

The parameter scheme and the corresponding code of TUV model can be found at:

https://www2.acom.ucar.edu/modeling/tuv-download

We also referred to He et al. (2023) to calculate the photolysis rate as following:

■ Photolysis rate

The photolysis rate of a given molecule X, J_X, is dependent on the incident actinic flux, $F(\lambda)$, the absorption cross-section, $\sigma(\lambda)$, and the quantum yield, $\phi(\lambda)$:

$$J_X = \int_{\lambda 1}^{\lambda 2} \sigma(\lambda)\phi(\lambda)F(\lambda)d\lambda$$

$\sigma(\lambda)$ and $\phi(\lambda)$ (both of the two parameters depend on wavelength and temperature) were retrieved from the MPI-Mainz UV/VIS Spectral Atlas (http://satellite.mpic.de/spectral_atlas). The actinic flux $F(\lambda)$ describes the total

energy pf photons incident on the unit sphere, which is calculated by integrating the radiance over all directions and can be expressed as:

$$F(\lambda) = \int_0^{2\pi} \int_{-\pi/2}^{\pi/2} L(\lambda, \theta, \varphi) \sin \theta d\theta d\varphi$$

$L(\lambda, \theta, \varphi)$ is spectral radiance (θ and φ are the zenith and azimuth angles, respectively).

Theoretical relationships between the actinic flux and the irradiance were presented to convert actinic flux from irradiance:

$$F(\lambda) = \left(\alpha(\lambda) + \left(\frac{1}{\cos(\theta)} - \alpha(\lambda) \right) \frac{E_{dir}(\lambda)}{E(\lambda)} \right) \times E(\lambda)$$

$\alpha(\lambda)$ is the spectral ratio of diffuse actinic flux to diffuse irradiance. $E_{dir}(\lambda)/E(\lambda)$ is the spectral ratio of direct to total irradiance. θ is the solar zenith angle. By definition, the spectral irradiance $E(\lambda)$ is the radiation incident on unit flat (usually horizontal) surface, which is calculated by integration of the radiance over a hemisphere and can be expressed as:

$$E(\lambda) = \int_0^{2\pi} \int_0^{\pi/2} L(\lambda, \theta, \varphi) \cos \theta \sin \theta d\theta d\varphi$$

The photolysis rate and actinic flux at different altitudes (h) can be described as:

$$F(h, \lambda) = \left(\alpha(h, \lambda) + \left(\frac{1}{\cos(\theta)} - \alpha(h, \lambda) \right) \frac{E_{dir}(\lambda)}{E(\lambda)} \right) \times E(h, \lambda)$$

■ Spectral irradiance at different altitudes

In the absence of actinic flux observation, it seems a promising method that the photolysis rate with acceptable uncertainty is obtained by calculating the actinic flux from the spectral irradiance. The solar spectral irradiance at different altitudes can be calculated as following:

$$E(h, \lambda) = E_{extra}(\lambda) \cdot e^{-\frac{C(\lambda) \cdot D(h)}{\cos \theta}}$$

$E_{extra}(\lambda)$ is solar spectral irradiance from extraterrestrial. $C(\lambda)$ represents the effect of wavelength on absorption coefficient (depend on wavelength and weather conditions). $D(h)$ reflects the influence of altitude on absorption coefficient and is defined as the ratio of atmospheric pressure at h km (P_h) to that at 0.0 km (P_0), i.e. $D(h) = P_h/P_0$. By conversion, $E(h, \lambda)$ can be calculated as following:

$$\ln E(h, \lambda) = \left(\ln E(0, \lambda) - \ln E_{extra}(\lambda) \right) \times \frac{P_h}{P_0} + \ln E_{extra}(\lambda)$$

P_0 came from ERA5, while P_h can be converted from height by barometric height formula. Solar spectral irradiance at ground surface $E(0, \lambda)$ can be calculated using

total surface solar radiation and MAX-DOAS measured spectra.

■ $\alpha(h,\lambda)$ and $E_{dir}(h,\lambda)/E(h,\lambda)$ at different altitudes

$\alpha(h,\lambda)$ is the spectral ratio of diffuse actinic flux to diffuse irradiance at different altitudes, which were affected by different factors (e.g. solar zenith angle and wavelength). Considering the almost constant surface albedo during the campaign, the impacts of solar zenith angle on the change of $\alpha(0,\lambda)$ is small and could be ignored. The effect of wavelength can be estimated as following equation. As discussed previously, due to lack of studies on $\alpha(0,\lambda)$ at different altitudes, we have to apply it to higher altitudes in this study.

$$\alpha(h,\lambda)=\frac{1}{0.5-(\lambda-300)/1000}$$

$E_{dir}(h,\lambda)/E(h,\lambda)$ is the spectral ratio of direct irradiance to total irradiance at different altitudes. The error of $E_{dir}(h,\lambda)/E(h,\lambda)$ has relatively less influence on the photolysis rate, especially during the midday with low solar zenith angle. Since the solar radiation can be defined as the total energy of the full spectral irradiance integral, we assume that $E_{dir}(h,\lambda)/E(h,\lambda)$ and $G_{dir}(h)/G(h)$ were approximately equal in this research, and further can be quantified by following equation according to the national guidelines (GB/T 37525-2019).

$$\frac{E_{dir}(h,\lambda)}{E(h,\lambda)}=\frac{G_{dir}(h)}{G(h)}=1-f(k,h)$$

$G_{dir}(h)$ is direct solar radiation ($G_{dir}(h)=\int_{0}^{3000}E_{dir}(h,\lambda)d\lambda$). $G(h)$ is total solar radiation ($G(h)=\int_{0}^{3000}E(h,\lambda)d\lambda$). $f(k,h)$ represents the ratio of diffuse solar radiation to total solar radiation.

$$f(k,h)=\begin{cases}1.0-0.249\cdot k(h) & 0\le k(h)\le 0.35\\ 1.557-1.84\cdot k(h) & 0.35\le k(h)\le 0.75\\ 0.177 & k(h)\ge 0.75\end{cases}$$

$$k(h)=G(h)/G_{extra}$$

where $k(h)$ is clearness coefficient. n is day of year (DOY) and S_0 is the solar constant of 1366.1 W·m^{-2}; G_{extra} is extraterrestrial solar radiation

$(G_{extra} = S_0 \cdot (1 + 0.033 \cos\left(\dfrac{360n}{365}\right)) \cdot \cos\theta)$.

Total solar radiation at differently altitudes $G(h)$ can be estimated by the following equation.

$$G(h) = G_{extra} \cdot e^{-\frac{C \cdot D(h)}{\cos\theta}}$$

where C represents absorption coefficient (Depend on weather conditions). With conversion, it can be calculated by following equation.

$$\ln G(h) = \left(\ln G(0) - \ln G_{extra} \right) \times \frac{P_h}{P_0} + \ln G_{extra}$$

The $G(0)$ can be observed by meteorological instruments or reanalysis data.

The correlation coefficients (R) between J(HONO) calculated using above method and J(HONO) simulated by TUV model at different altitude were **larger than 0.91**. It indicates that the HONO photolysis rates simulated by the TUV model are accurate under clean and cloud-free days. We also plan to optimize the parameterization scheme of WRF-Chem to simulate OH in the future.

In addition, the calculated OH were validated with measured OH, but the specific discussion will be organized in a separate study.

Specific comments

1. Authors' affiliations and addresses should be numbered in the appearance order of their names, to avoid the misunderstanding of academic misconduct.

Re: Thanks for your great comments. We have modified this section as following:

Chengzhi Xing[1], Cheng Liu[1,2,3,4,*], Chunxiang Ye[5,*], Jingkai Xue[6], Hongyu Wu[6], Xiangguang Ji[7], Jinping Ou[8], and Qihou Hu[1]

[1] Key Lab of Environmental Optics & Technology, Anhui Institute of Optics and Fine Mechanics, Hefei Institutes of Physical Science, Chinese Academy of Sciences, Hefei, 230031, China
[2] Department of Precision Machinery and Precision Instrumentation, University of Science and Technology of China, Hefei, 230026, China
[3] Center for Excellence in Regional Atmospheric Environment, Institute of Urban Environment, Chinese Academy of Sciences, Xiamen, 361021, China
[4] Key Laboratory of Precision Scientific Instrumentation of Anhui Higher Education Institutes, University of Science and Technology of China, Hefei, 230026, China
[5] College of Environmental Sciences and Engineering, Peking University, 100871 Beijing
[6] School of Environmental Science and Optoelectronic Technology, University of Science and Technology of China, Hefei, 230026, China
[7] Institute of Physical Science and Information Technology, Anhui University, Hefei, 230601, China
[8] The Department of Health Promotion and Behavioral Sciences, School of Public Health, Anhui Medical University, Hefei, 230032, China

*Corresponding author. E-mail: chliu81@ustc.edu.cn; c.ye@pku.edu.cn

2. Line 4: The full name should be given when the abbreviation ("MAX-DOAS") first appears. Please modify similar problems elsewhere (For example, "TUV" in Line 100).

Re: Thanks for your great comments. We have checked this problem in the full

manuscript, and have made the following modifications.

(1) In this study, we conducted multi-axis differential optical absorption spectroscopy (MAX-DOAS) measurements at Nam Co, the central TP, to observe the vertical profiles of aerosol, water vapor (H_2O), NO_2, HONO and O_3 from May to July 2019.

(2) The maximum values of monthly averaged aerosol (0.17 km^{-1}) and O_3 (66.71 ppb) occurred on May, H_2O (3.68×10^{17} molec cm^{-3}) and HONO (0.13 ppb) appeared on July, while NO_2 (0.39 ppb) occurred on June at 200-400 m layer.

(3) H_2O, HONO and O_3 all exhibited a multi-peak pattern, and aerosol appeared a bi-peak pattern for their averaged diurnal variations.

(4) The maximum values of HONO/NO_2 appeared around H_2O being 1.0×10^{17} molec cm^{-3} and aerosol being lager 0.15 km^{-1} under 1.0 km, and the maximum values usually accompanied with H_2O being $1.0\text{-}2.0 \times 10^{17}$ molec cm^{-3} and aerosol being lager 0.02 km^{-1} at 1.0-2.0 km.

(5) The TP spans 2.5 million square kilometers with an average altitude of over 4000 m.

(6) In addition, scientists are relying on advancements in satellite remote sensing technology, such as the tropospheric monitoring instrument (TROPOMI), the ozone monitoring instrument (OMI), the moderate-resolution imaging spectroradiometer (MODIS) and the cloud-aerosol lidar and infrared pathfinder satellite observation (CALIPSO), to monitor the spatial and temporal evolutions of atmospheric composition on the TP.

(7) MAX-DOAS has the technical advantage of low-cost continuous observation of multiple atmospheric components (i.e. aerosol, O_3 and their precursors).

(8) Lin et al. (2008) and Ye (2019) also confirmed that the high OH over the TP is mainly related to the reaction between $O(^1D)$ and H_2O.

(9) Therefore, a hypothesis of "strong AOC over the TP" was put forward. Previous studies pointed out that HONO also play an important role in AOC at low-altitude areas, and its contribution to OH can reach 40-60%, and even more than 80% in the early morning.

(10) Our previous study operated at the Qomolangma Atmospheric and Environmental Observation and Research Station, Chinese Academy of Sciences (QOMS-CAS) revealed that the HONO mainly distributed in the lower PBL and peaked in summer with 1.11 ppb, which is comparable to the average level of HONO in other low-altitude areas.

(11) Afterwards, the contributions of O_3 and HONO to OH in the vertical space were discussed through the tropospheric ultraviolet and visible (TUV) radiative transfer model and MAX-DOAS measurements.

(12) Moreover, due to the summertime huge evaporation from Nam Co lake, the atmospheric H_2O around CAS (NAMORS) is more abundant than in other areas of the TP, resulting in lush grass vegetation and making the area around this station an important summertime pasture.

(13) Averaged spatial distributions of AOD, NO_2 and O_3 monitored by satellite from May to July 2019 are shown in Fig. S1.

(14) The differential slant column densities (DSCDs) of O_4, H_2O, NO_2, HONO and O_3

were retrieved using QDOAS software (http://uvvis.aeronomie.be/software/QDOAS/) developed by Royal Belgian Institute for Space Aeronomy (BIRA-IASB).

(15) In this study, the initial a priori profile shape of above five species was set to exponential decreasing shape, and the AOD and vertical column densities (VCDs) simulated by weather research and forecasting model coupled chemistry (WRF-Chem) were also used as initial input a priori information to constrain the retrieval process.

(16) The calculation of photolysis rates of HONO and O_3 used TUV radiation model based on a full FORTRAN code, and this model usually runs accurately in clean, sunny and cloudless days.

(17) The initial input parameters were as follows: the AOD at 361 nm was derived from aerosol extinction profiles measured by MAX-DOAS.

(18) The PBL height was simulated using WRF with spatiotemporal resolutions of 20X20 km^2 and 1.0 hour (detailed configurations in Sect. S2 of the supplement).

(19) Moreover, the large-scaled spatial distributions of AOD, O_3 and NO_2 over CAS (NAMORS) were monitored by Himawari-8, OMI and TROPOMI, respectively.

(20) Figure 4. Time series of (a) aerosol extinction, (b) H_2O, (c) NO_2, (d) HONO, and (e) O_3 monitored by MAX-DOAS at 0-0.2, 0.4-0.6, 0.8-1.0, 1.2-1.4 and 1.6-1.8 km five height layers from 01 May to 09 July 2019.

(21) Figure 5. Vertical profiles of (a) aerosol extinction, (b) H_2O, (c) NO_2, (d) HONO, and (e) O_3.

(22) As shown in Figure 8, scatter plots between HONO/NO_2 and H_2O were illustrated.

(23) This phenomenon of HONO/NO_2 firstly increasing and then decreasing with the increasing of H_2O (or relative humidity) was usually found in low-altitude areas in previous studies.

(24) When the H_2O was greater than above mentioned critical values at different heights, HONO/NO_2 gradually decreased, which was related to the efficient uptake of HONO and the decrease of NO_2 reactivity with the increase of H_2O. That indicated H_2O has significant enhancement for the conversion rate of NO_2 to HONO.

(25) The scatter plots between HONO and NO_2 at above five layers (Figure S6) also confirmed the possibility of the NO_2 heterogeneous reaction to generate HONO on the TP, and the contribution of atmospheric H_2O and aerosol extinction to this process.

(26) Figure 8. Scatter plots between HONO/NO_2 and H_2O colored by aerosol extinction at (a) 0.0-0.2 km, (b) 0.4-0.6 km, (c) 0.8-1.0 km, (d) 1.2-1.4 km, (and e) 1.6-1.8 km from 1st May to 9th July 2019.

(27) We found that HONO/NO_2 first increasing and then decreasing with the increasing of H_2O. The maximum value of HONO/NO_2 appeared around H_2O being around 1.0X10^{17} molec cm^{-3} under 1.0 km, and being around 1.0-2.0X10^{17} molec cm^{-3} at 1.0-2.0 km height layer.

3. Line 27 and Line 575: The references' format is not consistent between the text and the reference section, which leads to poor readability of the manuscript for review. Please modify all the similar problems.

Re: Thanks for your great comments. We have made following modifications.

[1] Ma, Y., Hu, Z., Xie, Z., Ma, W., Wang, B., Chen, X., Li, M., Zhong, L., Sun, F., Gu, L., Han, C., Zhang, L., Liu, X., Ding, Z., Sun, G., Wang, S., Wang, Y., Wang, Z.: A

long-term (2005-2016) dataset of hourly integrated land-atmosphere interaction observations on the Tibetan Plateau, Earth Syst. Sci. Data, 12, 2937-2957, doi.org/10.5194/essd-12-2937-2020, 2020.

[2] Fang, B., Zhao, W., Xu, X., Zhou, J., Ma, X., Wang, S., Zhang, W., Venables, D. S., Chen, W.: Portable broadband cavity-enhanced spectrometer utilizing Kalman filtering: application to real-time, in situ monitoring of glyoxal and nitrogen dioxide, Opt. Express, 25, 26910-26922, doi.org/10.1364/OE.25.026910, 2017.

[3] Bessho, K., Date, K., Hayashi, M., Ikeda, A., Imai, T., Inoue, H., Kumagai, Y., Miyakawa, T., Murata, H., Ohno, T., Okuyama, A., Oyama, R., Sasaki, Y., Shimazu, Y., Shimoji, K., Sumida, Y., Suzuki, M., Taniguchi, H., Tsuchiyama, H., Uesawa, D., Yokota, H., and Yoshida, R.: An Introduction to Himawari-8/9-Japan's New-Generation Geostationary Meteorological Satellites, J. Meteorol. Soc. Jan., 94, 151-183, doi: 10.2151/jmsj.2016-009, 2016.

[4] Veefkind, J.P., de Haan, J.F., Brinksma, E.J., Kroon, M., and Levelt, P.F.: Total Ozone From the Ozone Monitoring Instrument (OMI) Using the DOAS Technique, IEEE T. Geosci. Remote Sens., 44, 1239-1244, doi:10.1109/TGRS.2006.871204, 2004.

[5] Boos, W. R. and Kuang, Z.: Dominant control of the South Asian monsoon by orographic insulation versus plateau heating, Nature, 463, 218–222, doi:10.1038/nature08707, 2010.

[6] Yanai, M., Li, C., and Song, Z.: Seasonal Heating of the Tibetan Plateau and Its Effects on the Evolution of the Asian Summer Monsoon, J. Meteorol. Soc. Jpn. Ser. II, 70, 319–351, doi:10.2151/jmsj1965.70.1B_319, 1992.

[7] Hsu, H-H., and Liu, X.: Relationship between the Tibetan Plateau heating and East Asian summer monsoon rainfall, Geophys. Res. Lett., 30, 2066, doi.org/10.1029/2003GL017909, 2003.

[8] Barnett, T. P., Adam, J. C., and Lettenmaier, D. P.: Potential impacts of a warming climate on water availability in snow-dominated regions, Nature, 438, 303–309, doi:10.1038/nature04141, 2005.

[9] Bolch, T., Kulkarni, A., Kaab, A., Huggel, C., Paul, F., Cogley, J. G., Frey, H., Kargel, J. S., Fujita, K., Scheel, M., Bajracharya, S., and Stoffel, M.: The State and Fate of Himalayan Glaciers, Science, 336, 310–314, doi:10.1126/science.1215828, 2012.

[10] Kang, S., Huang, J., Wang, F., Zhang, Q., Zhang, Y., Li, C., Wang, L., Chen, P., Sharma, C., Li, Q., Sillanpaa, M., Hou, J., Xu, B., and Guo, J.: Atmospheric Mercury Depositional Chronology Reconstructed from Lake Sediments and Ice Core in the Himalayas and Tibetan Plateau, Environ. Sci. Technol., 50, 2859–2869, doi:10.1021/acs.est.5b04172, 2016.

[11] Rawat, P., and Naja, M.: Remote sensing study of ozone, NO_2, and CO: some contrary effects of SARS-CoV-2 lockdown over India, Environ. Sci. Pollut. Res., 29, 22515-22530, doi:10.1007/s11356-021-17441-2, 2022.

[12] Yang, K., Koike, T., and Yang, D.: Surface flux parameterization in the Tibetan Plateau, Bound.-Lay. Meteorol., 106, 245–262, doi:10.1023/A:1021152407334, 2003.

[13] Zhang, J., Xia, X., and Wu, X.: First in situ UV profile across the UTLS accompanied by ozone measurement over the Tibetan Plateau, J. Environ., Sci., 98, 71–76, doi:10.1016/j.jes.2020.05.020, 2020.

[14] Fang, X., Li, T., Ban, C., Wu, Z., Li, J., Li, F., Cen, Y., and Tian, B.: A mobile differential absorption lidar for simultaneous observations of tropospheric and stratospheric ozone over Tibet, Opt. Express, 27, 4126–4139, doi:10.1364.OE.27.004126, 2019.

[15] Yang, J., Kang, S., Hu, Y., Chen, X., Rai, M.: Influence of South Asian biomass burning on ozone and aerosol concentrations over the Tibetan Plateau, Adv. Atmos. Sci., 39, 1184-1197, doi:10.1007/s00376-022-1197-0, 2022.

4. Line 26-38: This paragraph is not closely related to the key ideas of this paper. Moreover, the last sentence is lack of proper deduction.

Re: Thanks for your great comments. We try to make some explanations and modifications as following:

(1) The purpose of this paragraph is to emphasize the importance of the TP on climate change and reginal air pollution due to its special location and geographic features. It amounts to an explanation of the context of this study.

(2) We have rewritten this paragraph as "The TP spans 2.5 million square kilometers with an average altitude of over 4000 m. Therefore, the TP is called the "Third Pole" of the earth (Ma et al., 2020; Kang et al., 2022). It is the home to tens of thousands of glaciers and nourishes more than 10 of Asia's rivers, thus it also acts the role of "Water Tower of Asia" (Qu et al., 2019; Ma et al., 2022). Due to its special topography, the TP is the heat source of atmosphere due the strong solar radiation, which as the driven force to profoundly affect the regional atmospheric circulation, global weather conditions and climate change (Yanai et al., 1992; Boos et al., 2010; Chen et al., 2015; Liu et al., 2022; Zhou et al., 2022). Monsoon rainfall in Asia, flood over the Yangtze River valley, and El Niño in the Pacific Ocean are strongly associated with the TP (Hsu et al., 2003; Li et al., 2016; Lei et al., 2019). In addition, the cyclone circulations caused by the TP heat source also can inhibit the diffusion of atmospheric pollutants in the areas around the TP, such as the Sichuan Basin, causing regional pollution (Zhang et al., 2019). Therefore, observations of the atmospheric species on the TP are essential to enhance the in-depth understanding of its atmospheric physicochemical processes."

5. Line 39-73: This paragraph is lack of many key references for MAX-DOAS observations over the Tibetan Plateau. It is not appropriate to cite only the studies from author's group.

Re: Thanks for your great comments. However, the reality is that there are very few reports on the atmospheric environment of the Tibetan Plateau based on MAX-DOAS. These studies all have been carried out by Chinese researchers. The reference list is as following:

[1] Cheng, S., Pu, G., Ma, J., Hong, H., Du, J., Yudron, T., Wagner, T.: Retrieval of tropospheric NO_2 vertical column densities from ground-based MAX-DOAS measurements in Lhasa, a city on the Tibetan Plateau, Remote Sens., 15, 4689, 2023.

[2] Cheng, S., Ma, J., Zheng, A., Gu, M., Donner, S., Donner, S., Zhang, W., Du, J., Li, X., Liang, Z., Lv, J., Wagner, T.: Retrieval of O_3, NO_2, BrO and OClO columns from ground-based zenith scattered light DOAS measurements in summer and autumn over

the Northern Tibetan Plateau, Remote Sens., 13, 4242, 2021.

[3] Ma, J., Donner, S., Donner, S., Jin, J., Cheng, S., Guo, J., Zhang, Z., Wang, J., Liu, P., Zhang, G., Pukite, J., Lampel, J., Wagner, T.: MAX-DOAS measurements of NO_2, SO_2, HCHO, and BrO at the Mt. Waliguan WMO GAW global baseline station in the Tibetan Plateau, Atmos. Chem. Phys., 20, 6973-6990, 2020.

[4] Cheng, S., Cheng, X., Ma, J., Xu, X., Zhang, W., Lv, J., Bai, G., Chen, B., Ma, S., Ziegler, S., Donner, S., Wagner, T.: Mobile MAX-DOAS observations of tropospheric NO_2 and HCHO during summer over the Three Rivers' Source region in China, Atmos. Chem. Phys., 23, 3655-3677, 2023.

[5] Xing, C., Liu, C., Wu, H., Lin, J., Wang, F., Wang, S., Gao, M.: Ground-based vertical profile observations of atmospheric composition on the Tibetan Plateau (2017-2019), Earth Syst. Sci. Data, 13, 4897-4912, 2021.

[6] Li, M., Mao, J., Chen, S., Bian, J., Bai, Z., Wang, X., Chen, W., Yu, P.: Significant contribution of lightning NO_x to summertime surface O_3 on the Tibetan Plateau, Sci. Total Environ., 829, 154639, 2022.

Moreover, we have rewritten the related sentence as "MAX-DOAS has the technical advantage of low-cost continuous observation of multiple atmospheric components (i.e. aerosol, O_3 and their precursors) (Wang et al., 2018; Ma et al., 2020; Cheng et al., 2021; Xing et al., 2021; Li et al., 2022; Cheng et al., 2023a, 2023b).".

6. Line 75: The O_3 will be diluted when the air mass comes from clean source regions, such as marine atmosphere.

Re: Thanks for your great comments. We would like to make two statements about this problem as following:

The main point referred from Ye and Gao (1997) is that the strong convergent airflow formed under the combined action of monsoon, subtropical anticyclone and the airflow of subtropical westerlies could promote the accumulation of O_3 on the TP in summer. It is not that air mass coming from clean regions promote the increase of O_3 on the TP, but rather that the strong convergent airflow contributed by monsoon, subtropical anticyclone and the airflow of subtropical westerlies could promote the accumulation of O_3 on the TP. The strong convergent airflow not only promote the transport of high-concentration O_3 from the surrounding area to the TP but also inhibit the diffusion of O_3 from the TP to the outside.

Moreover, we retrieved the spatial distribution of tropospheric O_3 based on the issues raised by the reviewers (Figure R5). We could find that there are some areas with high O_3 values in the oceans, especially in the Indian Ocean and in the Bohai and Yellow Sea regions of China. The sources of O_3 with high values in these regions need to be further explored.

Reference: Ye, D. Z., and Gao, Y. X.: The meteorology of the Tibetan Plateau (in Chinese), 278pp., Science Press, Beijing, pp. 39-48, 1979.
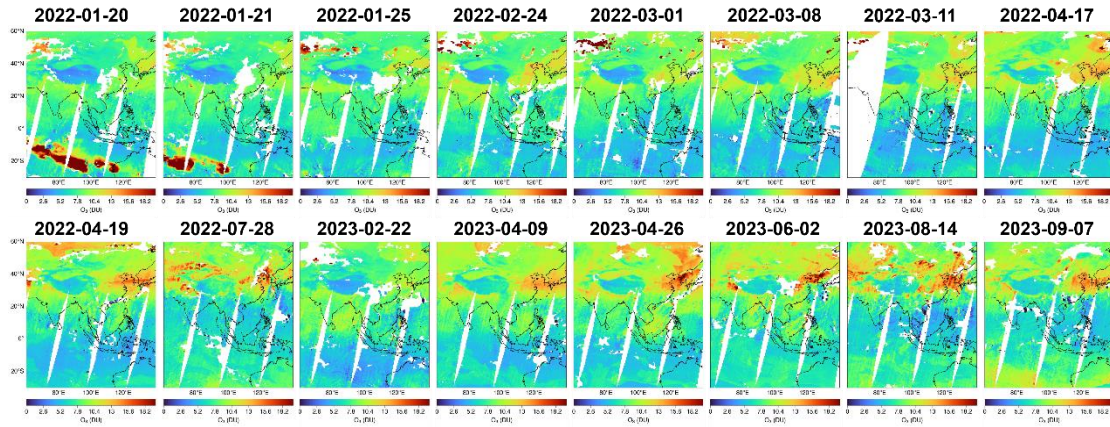
Figure R5. Spatial distributions of tropospheric O_3 monitored by TROPOMI.

7. Line 122: Again, sensitivity test and profile validation by independent data should be presented to confirm the reliability of retrieval results.

Re: Thanks for your great comments. We have reorganized this section as following:

2 Method and methodology

2.1 Site

2.2 Measurements

2.2.1 Instrument setup and spectral analysis

2.2.2 Vertical profile retrieval

2.2.3 Error analysis

In order to ensure the reliability of data, error analysis was carried out.

The error sources can be divided into four different types: smoothing error, noise error, forward model error, and model parameter error (Rodgers, 2004). However, in terms of this classification, some errors are difficult to be calculated or estimated. For example, the forward model error, which is caused by an imperfect representation of the physics of the system, is hard to be quantified due to the difficulty of acquiring an improved forward model. Given calculation convenience and contributing ratios of different errors in total error budget, we mainly took into account following error sources, which were smoothing and noise errors, algorithm error, cross section error, and uncertainty related to the aerosol retrieval (only for trace gas). In this study, we estimated the contribution of different error sources to the AOD and VCDs of trace gases, and near-surface (0–200 m) trace gases' concentrations and aerosol extinction coefficients (AECs), respectively. The detailed demonstrations and estimation methods are displayed below, and the corresponding varies errors are summarized in Table R1.

i.   Smoothing errors arise from the limited vertical resolution of profile retrieval. Noise errors denote the noise in the spectra (i.e., the error of DOAS fits). Considering the error of the retrieved state vector equaling the sum of these two independent errors, we calculated the sum of smoothing and noise errors on near-surface concentrations and column densities, which were 13 and 5 % for aerosols, 13 and 36 % for H_2O, 12 and 14 % for NO_2, 18 and 21 % for HONO, and 12 and 32 % for O_3, respectively.

j.   Algorithm error is denoted by the differences between the measured and simulated DSCDs. This error contains forward model error from an imperfect approximation

of forward function, parameter error of forward model, and other errors, such as detector noise (Rodgers, 2004). Algorithm error is a function of the viewing angle, and it is difficult to assign this error to each altitude. Thus, this error on the near-surface values and column densities is estimated through calculating the average relative differences between the measured and simulated DSCDs at the minimum and maximum elevation angle (except 90°), respectively (Wagner et al., 2004). In this study, we estimated these errors on the near-surface values and the column densities at 4 and 8 % for aerosols, 3 and 11 % for NO_2, and 20 and 20 % for HONO referring to Wang et al. (2017, 2020), 1 and 8 % for H_2O referring to Lin et al. (2020), and 6 and 10 % for O_3 referring to Ji et al. (2023), respectively.

k. Cross section error arises from the uncertainty in the cross section. According to Thalman and Volkamer, (2013), Lin et al. (2020), Vandaele et al. (1998), Stutz et al. (2000), and Serdyuchenko et al. (2014), we adopted 4, 3, 3, 5, and 2 % for O_4 (aerosols), H_2O, NO_2, HONO and O_3, respectively.

l. The profile retrieval error for trace gases is sourced from the uncertainty of aerosol extinction profile retrieval and propagated to trace gas profile. This error could be roughly estimated based on a linear propagation of the total error budgets of the aerosol retrievals. The errors of the learned four trace gases were roughly estimated at 14 % for VCDs and 10 % for near-surface concentrations, respectively.

The total uncertainty was the sum of all above errors in the Gaussian error propagation, and the error results were listed in Table R1. We found that the smoothing and noise errors played a dominant role in the total uncertainties of aerosol and trace gases. Moreover, improving the accuracy and temperature gradient of the absorption cross section is another important means to reduce the uncertainty of the vertical profiles in the future, especially for O_3.

Certainly, we also did independent validations. However, there was not other vertical observations during our campaign on the TP. Therefore, we did validations between in situ measurements and the bottom layer of MAX-DOAS profiles (Figure R1).

Moreover, we did vertical-profile validations in Shanghai and Beijing. As shown in Figure R2, we used Mie lidar to validate MAX-DOAS aerosol vertical profiles, and used balloon-based NO_2 profiles to validate MAX-DOAS NO_2 vertical profiles (Xing et al., 2017). The good agreement indicates the reliability of MAX-DOAS retrieved aerosol and NO_2 profiles.

As shown in Figure R3, the retrieved O_3 profiles were validated with tower-based O_3 profiles in Beijing. The correlation coefficients (R) between them on 2 m, 60 m, 160 m, and 280 m were 0.844, 0.864, 0.883 and 0.902, respectively.

8. Line 156: The cross sections are lack of references in Table 1.

Re: Thanks for your great comments. We have added the corresponding references as following.

[1] Aliwell, S. R., Van Roozendael, M., Johnston, P. V., Richter, A., Wagner, T., Arlander, D. W., Burrows, J. P., Fish, D. J., Jones, R. L., Tørnkvist, K. K., Lambert, J. C., Pfeilsticker, K., and Pundt, I.: Analysis for BrO in zenith-sky spectra: an intercomparison exercise for analysis improvement, J. Geophys. Res., 107, ACH 10-1–

ACH 10-20, https://doi.org/10.1029/2001JD000329, 2002.

[2] Vandaele, A. C., Hermans, C., Simon, P. C., Carleer, M., Colin, R., Fally, S., Mérienne, M. F., Jenouvrier, A., and Coquart, B.: Measurements of the NO_2 absorption cross section from 42000 cm^{-1} to 10000 cm^{-1} (238–1000nm) at 220 K and 294 K, J. Quant. Spectrosc. Ra., 59, 171–184, 1998.

[3] Meller, R. and Moortgat, G. K.: Temperature dependence of the absorption cross sections of formaldehyde between 223 and 323 K in the wavelength range 225–375 nm, J. Geophys. Res., 105, 7089–7101, 2000.

[4] Volkamer, R., Spietz, P., Burrows, J., Platt, U.: High-resolution absorption cross-section of glyoxal in the UV-vis and IR spectral ranges, J. Photochem. Photobiol. A Chem., 172, 35–46, 2005.

[5] Rothman, L. S., Gordon, I. E., Barbe, A., Benner, D. C., Bernath, P. E., Birk, M., Boudon, V., Brown, L. R., Campargue, A., Champion, J. P., Chance, K., Coudert, L. H., Dana, V., Devi, V. M., Fally, S., Flaud, J. M., Gamache, R. R., Goldman, A., Jacquemart, D., Kleiner, I., Lacome, N., Lafferty, W. J., Mandin, J. Y., Massie, S. T., Mikhailenko, S. N., Miller, C. E., Moazzen-Ahmadi, N., Naumenko, O. V., Nikitin, A. V., Orphal, J., Perevalov, V. I., Perrin, A., Predoi-Cross, A., Rinsland, C. P., Rotger, M., Simeckova, M., Smith, M. A. H., Sung, K., Tashkun, S. A., Tennyson, J., Toth, R. A., Vandaele, A. C., Vander Auwera, J.: The HITRAN 2008 molecular spectroscopic database, J. Quant. Spectrosc. Radiat. Transf., 110, 533–572, 2009.

[6] Fleischmann, O. C., Hartmann, M., Burrows, J. P., and Orphal, J.: New ultraviolet absorption cross-sections of BrO at atmospheric temperatures measured by time-windowing Fourier transform spectroscopy, J. Photoch. Photobio. A, 168, 117–132, 2004.

9. Line 165: Are only the HONO and O_3 data in clear sky condition used to calculate the photolysis rates. If so, there may be many missing data in summer due to clouds over the TP. This information should be explicitly mentioned in section 4.1.

Re: Thanks for your great comments.

The cloud parameters are important and complex factors influencing the photolysis rates of HONO and O_3. Inaccurate evaluation of cloud parameters will increase the uncertainty of above photolysis rates. In order to remove the misunderstanding that this uncertainty introduces into the assessment of AOC by HONO and O_3, we judged the cloud coverage firstly during our measurements. As shown in Figure R6 (a), we develop a cloud classification method based on the diurnal variations of Color Index (CI=I_{330}/I_{360}). To ensure a sufficient amount of valid data, we chose sunny and cloudless days to analyze the photolysis rates of HONO and O_3. Only the cloud coverage scenario of *II* in Fig. R6 (b) was masked. In this study, the validity of the data was more than 70%.
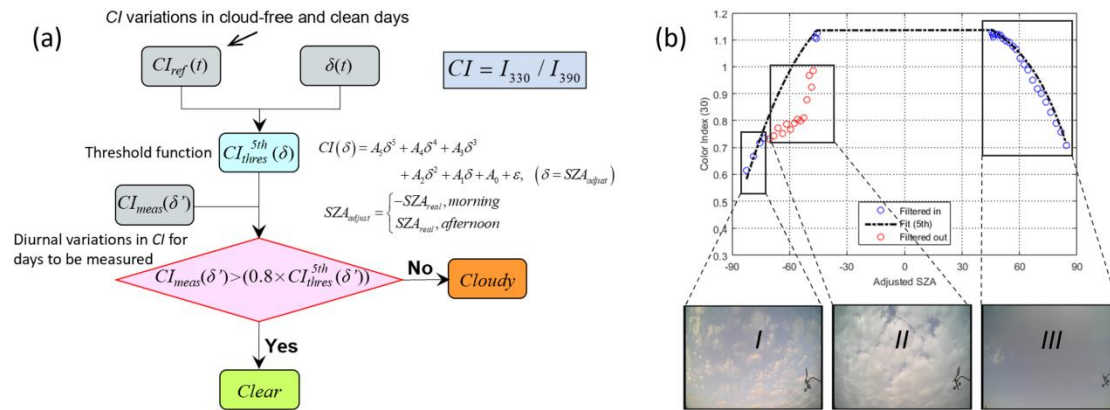
Figure R6. (a) Color Index cloud classification algorithm process. (b) Example of cloud classification.

The information was mentioned in section 2.3 (TUV model), but we have enriched the relevant information in the revised manuscript.

"In order to ensure the accuracy of model running, we only selected data in sunny and cloudless days. Moreover, we developed a cloud classification method based on the diurnal variations of Color Index ($CI=I_{330}/I_{360}$) in Figure S2."

10. Line 177: Please add references.

Re: Thanks for your great comments. We have rewritten this sentence as following:

"Moreover, the calculated backward trajectories were clustered into three groups using Ward's variance method and Angle Distance algorithm (Ward 1963; Wang et al., 2006)."

References

[1] Ward Jr, J. H.: Hierarchical grouping to optimize an objective function, J. Am. Stat. Assoc., 58, 236-244, 1963.

[2] Wang, Y., Zhang, X., Arimoto, R.: The contribution from distant dust sources to the atmospheric particulate matter loading at XiAn, China during spring, Sci. Total Environ., 368, 875-883, 2006.

11. Line 204-207: With respect to the enhancement of AOD during 15:00-17:00, the explanations are far-fetched. The daytime AOD diurnal variations at other time are probably affected by the long-range transport of aerosol and local anthropogenic sources (such as cooking in the morning).

Re: Thanks for your great comments. In Figure 4, we could find that the aerosol was mainly distributed under 200 m. Therefore, we simulated the wind information under 200 m at the measurement site. Seven height layers under 200 m (11 m, 36 m, 62 m, 83 m, 105 m, 125 m and 156 m) were selected. As shown in Figure R7, the wind speed was usually elevated after 15:00. It is very similar to the diurnal variation trend of the AOD. It indicates that long range transport and short range transport should be an important source of aerosol at our measurement site. We have modified this section as following:

"*Subsequently, the AOD increased significantly, reaching maximum values during 15:00-17:00 (average of 0.107 km^{-1}), which was about 1.408 times the diurnal average value. Considering the diurnal variation of wind speed (Figure S3), such an enhancement of AOD may be related to the long-range transport of aerosol from*

southern Asia (Yang et al., 2020; Bi et al., 2023). Moreover, 15:00-17:00 was the active time of tourists and local residents (i.e. cooking), and these kinds of anthropogenic sources contributed to the atmospheric AOD of NAMORS through short-distance transport (Yin et al., 2017; Zhang et al., 2017).".
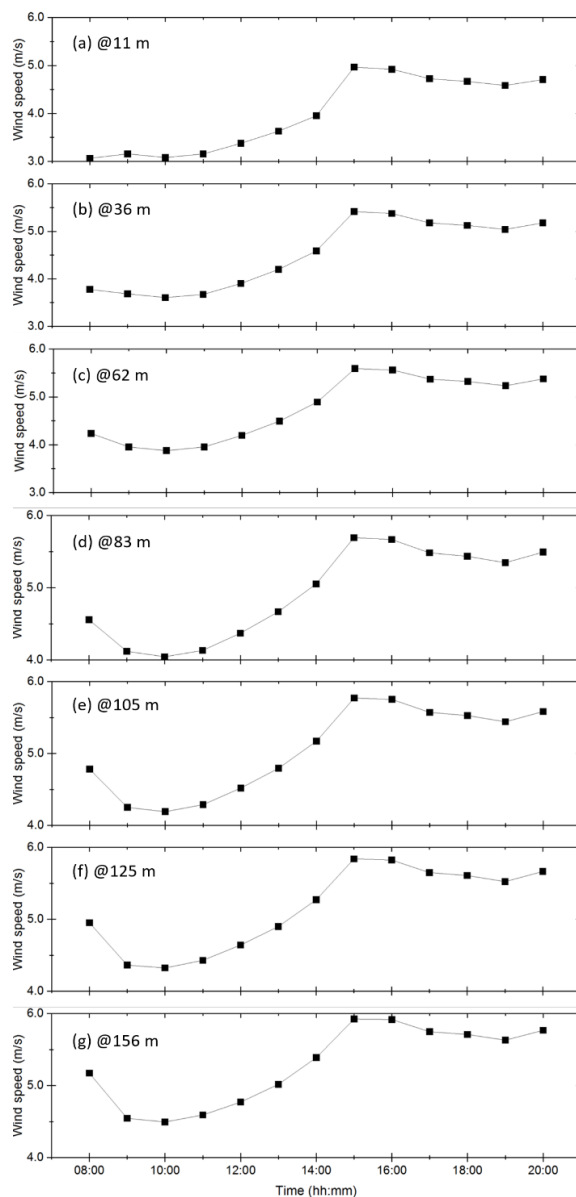

Figure R7. Wind speed at seven different height layers at the measurement site during the measurements.

12. Line 215: The manuscript selected 5 height layer to analyze temporal and vertical variations of atmospheric components. But why are the five height layers "typical"? The separate layers reduce the vertical resolution of retrieval results. It is better to investigate the daily variations through vertical profiles themselves. Please modify all the similar problems at other sections.

Re: Thanks for your great comments.

Figure R8 showed the diurnal variation of PBL. We could find that the maximum values of PBL (~2.0 km) at our measurement site appeared at 11:00-17:00, a relatively long

period. Considering that the pollutants were mainly distributed within the PBL, five heights under 2.0 km were selected to analyze the variations of several pollutants (aerosol, H_2O, NO_2, HONO and O_3) throughout the observation period.

There may be a misunderstanding. The purpose of Figure 4 is to show the variations of pollutants within the PBL during the observation period. ***We used the daily mean values of the different pollutants.*** In addition, the average diurnal variation of different pollutants was depicted in Figure 5.
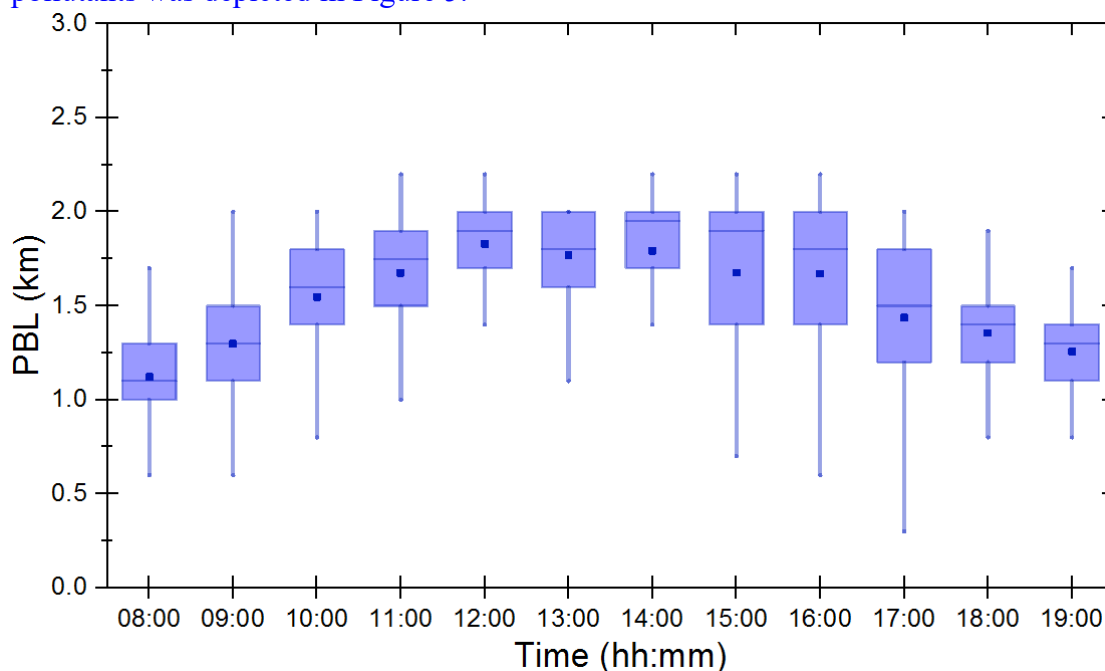
Figure R8. The diurnal variation of PBL in Nam Co from May to July 2019. The top and bottom of the box represented 75th and 25th percentiles, respectively. The lines and dots within the boxes were the median and mean, respectively.

We have rewritten these sentences as following:

"As shown in Figure S4, the diurnal variation of PBL in Nam Co from May to July 2019 was lower in the early morning and late afternoon, but higher between 11:00 and 17:00, a relatively long period, with the maximum PBL larger than 2.0 km. Zhang et al. (2017) and Yang et al., (2017) also reported that the PBL in Nam Co was usually larger than 1.0 km during daytime in spring and summer. In order to investigate the height-dependent variations of aerosol, H_2O, NO_2, HONO and O_3 within the PBL during the measurements, five height layers under the PBL (0.0-0.2 km, 0.4-0.6 km, 0.8-1.0 km, 1.2-1.4 km and 1.6-1.8 km) were thus selected."

"Figure 4. Time series of daily averaged (a) aerosol extinction, (b) H_2O, (c) NO_2, (d) HONO, and (e) O_3 monitored by MAX-DOAS at 0-0.2, 0.4-0.6, 0.8-1.0, 1.2-1.4 and 1.6-1.8 km five height layers from 01 May to 09 July 2019."

13. Line 224-225, 228-229: The explanations are lack of proper deduction.

Re: Thanks for your great comments.

"*That indicated that the aerosol was usually local-emitted at the surface, and the occasionally appearance of strong aerosol extinction at 0.4-0.6 km, such as 13th and 30th June, was associated with long-range transport from south Asia.*"
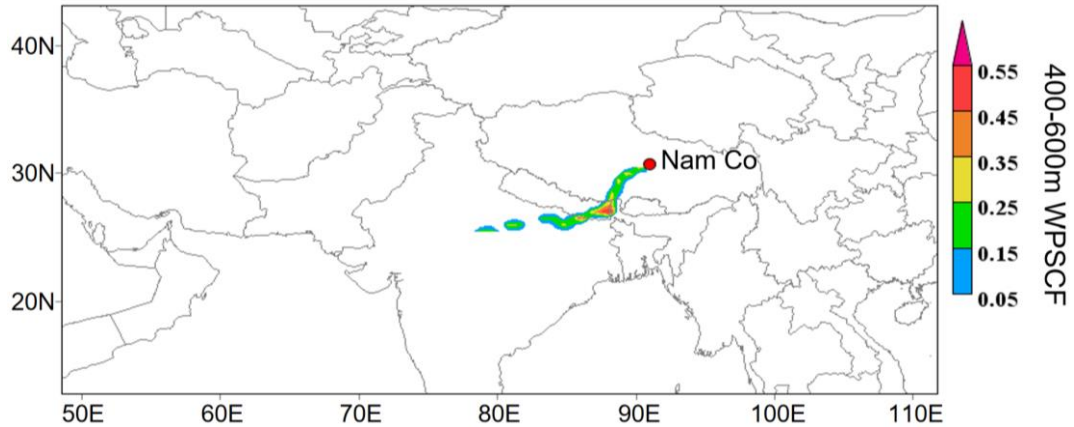
Figure R9. Spatial distribution of WPSCF values for aerosol at 400-600 m layer on 13th and 30th June.

In order to determine the potential source locations of aerosol at 400-600 m layer, the WPSCF model was used. As shown in Figure R9, the maximum values of WPSCF for aerosol at 400-600 m layer (> 0.45) was mainly from Nepal and the north of India.

"The average concentration of H_2O at 0.0-0.2 km was $2.35×10^{17}$ molec cm^{-3}, and the ratios of H_2O at 0.4-0.6 km, 0.8-1.0 km, 1.2-1.4 km and 1.6-1.8 km to those at 0.0-0.2 km were 83.40%, 68.08%, 50.64% and 35.74%, respectively, which should attribute to the transport of H_2O from Indian Ocean during the monsoon and the elevated evaporation from Nam Co lake to lead to its not obvious vertical gradient."
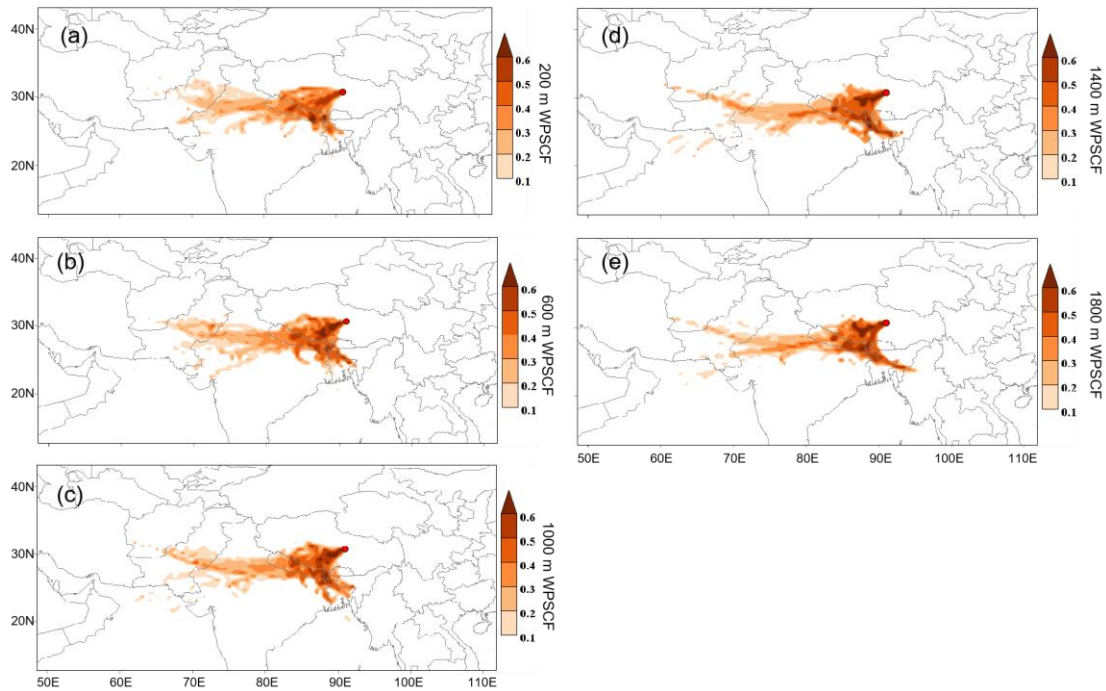

Figure R10. Spatial distributions of WPSCF values for H2O at (a) 200 m, (b) 600 m, (c) 1000 m, (d) 1400 m, and (e) 1800 m height layers from 01st May to 09th July 2019 over CAS (NAMORS).

In order to determine the potential source locations of H_2O under PBL, the WPSCF model was used. As shown in Figure R10, we could find that H_2O was mainly from south Asia, especially above 1000 m, driven by the Indian Ocean monsoon.

14. Line 233-234: As a short-life atmospheric component, can the NO_x around Mt. Tanggula transport to the observation site? Does the transport effect affect the NO_2 at the bottom layer? The causes of elevated NO_2 layer are probably complex.

Re: Thanks for your great comments.

NO_2 mainly sourced from primary emission and reginal transport in the atmosphere. The primary sources of NO_2 include traffic, industrial and residential emissions. However, as shown in Figure R11, there are few primary emission sources around our measurement site. The largest potential area with high NO_2 concentrations is from Dangxiong country, but there is ~34 km between the measurement site and Dangxiong country, and separated by the Mt. Tanggula. In addition, previous studies have reported that high NO_x production was due to photochemical reactions on the snow surface of the Tibetan Plateau (Fisher et al., 2005; Lin et al., 2021). Figure R11 also told us that the closest distance between the measurement site and the icy summit of Mt. Tanggula is only ~7.5 km. Therefore, we cannot exclude the possibility that NO_2 was transported from the Mt. Tanggula. NO_2 profile also showed a Gaussian shape, with maximum values appeared at 300-400 m layer. This is also a distinguishing feature of transport contributions for NO_2. Near-surface NO_2 concentrations at the measurement site were not high during the observation period.

Figure R11. Geographical location of CAS (NAMORS) and around environment. Moreover, we also did WPSCF analysis (Figure R12), and the WPSCF passing through Mt. Tanggula showed high values at 300-400 m layer, especially at 400 m (> 0.3). It indicated that the important contribution to NO_x from ice and snow on the top of Mt. Tanggula under strong ultraviolet radiation.
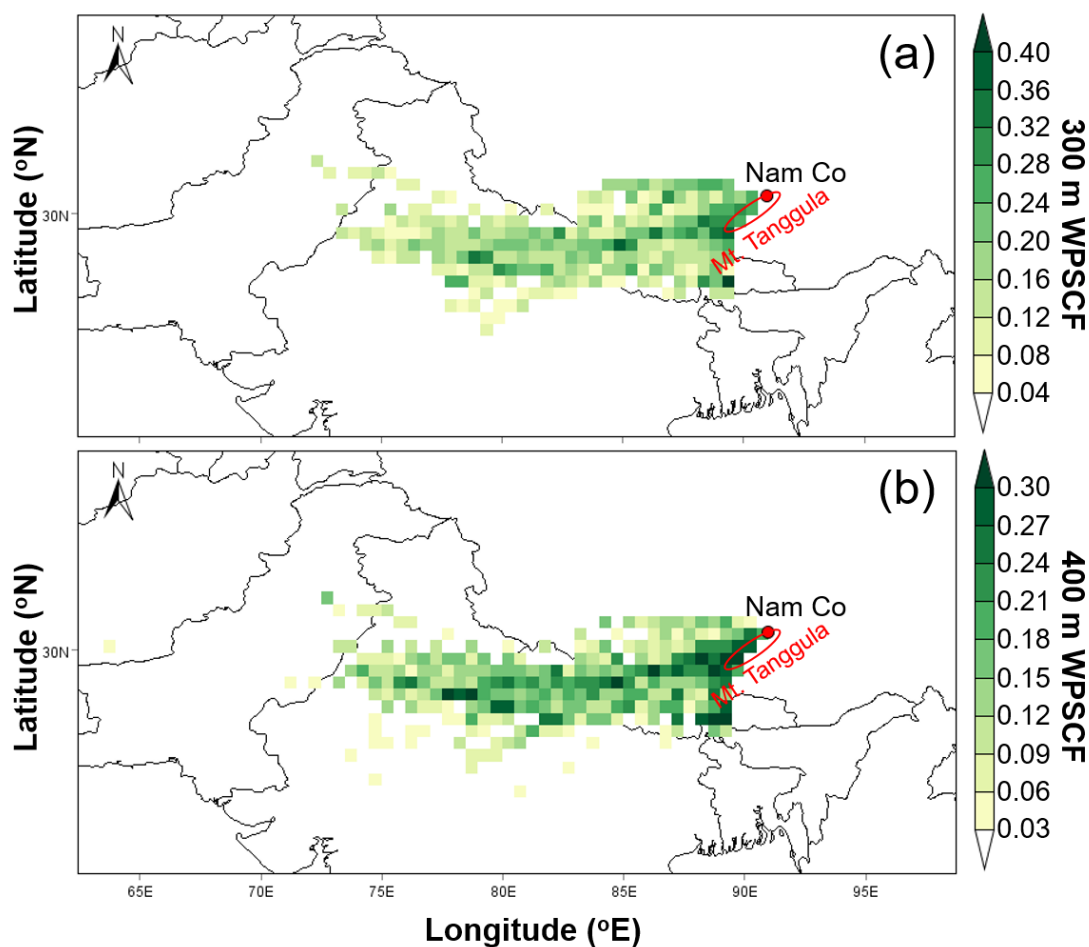
Figure R12. Spatial distributions of 24-h WPSCF values for NO_2 at (a) 300 m, and (b) 400 m height layers from 01 May to 09 July 2019 over CAS (NAMORS).

15. Line 240-243: The vertical distributions of O_3 in the lower tropospheric layer are complex over the Tibetan Plateau. Why does the manuscript describe the "exponential shape" derived from previous studies here? The "exponential shape" is not consistent with the relatively uniform vertical variation of O_3 in this study.

Re: Thanks for your great comments.

The purpose of describing the exponential shape of O_3 profiles reported in previous studies was to show that the shape of O_3 profiles in Nam Co observation was credible. The O_3 profiles showed in Figure R13 were all from Tibetan Plateau measured by satellite, O_3 lidar and ozonesonde, especially for Lahsa and Yangbajing, which were closed to Nam Co. The height ranges presented in each of the plots in Figure R13 are not consistent, but the O_3 profiles monitored by different means below 4.0 km basically show an approximate exponential shape. It is possible that the different heights in these plots of Figure R7 created a visual misjudgment for the reviewer. We apologize for this. Moreover, due to the limited vertical resolution of MAX-DOAS O_3 profiles, the limited degrees of freedom and the constraints of the radiative transfer model caused by O_3 profile retrieval algorithm, the detailed structure of O_3 at different vertical altitudes may be missing, but it essentially characterized the vertical distribution of the O_3 profile in Nam Co.

We have rewritten these sentences as "The vertical gradient of O_3 concentration was also not obvious, which was associated with its vertical mixing and photochemical production. As shown in Figure S5, the corresponding TROPOMI O_3 profiles in Nam Co and O_3 profiles measured by lidar and ozonesonde around Nam Co reported in several previous studies also exhibited an exponential shape".
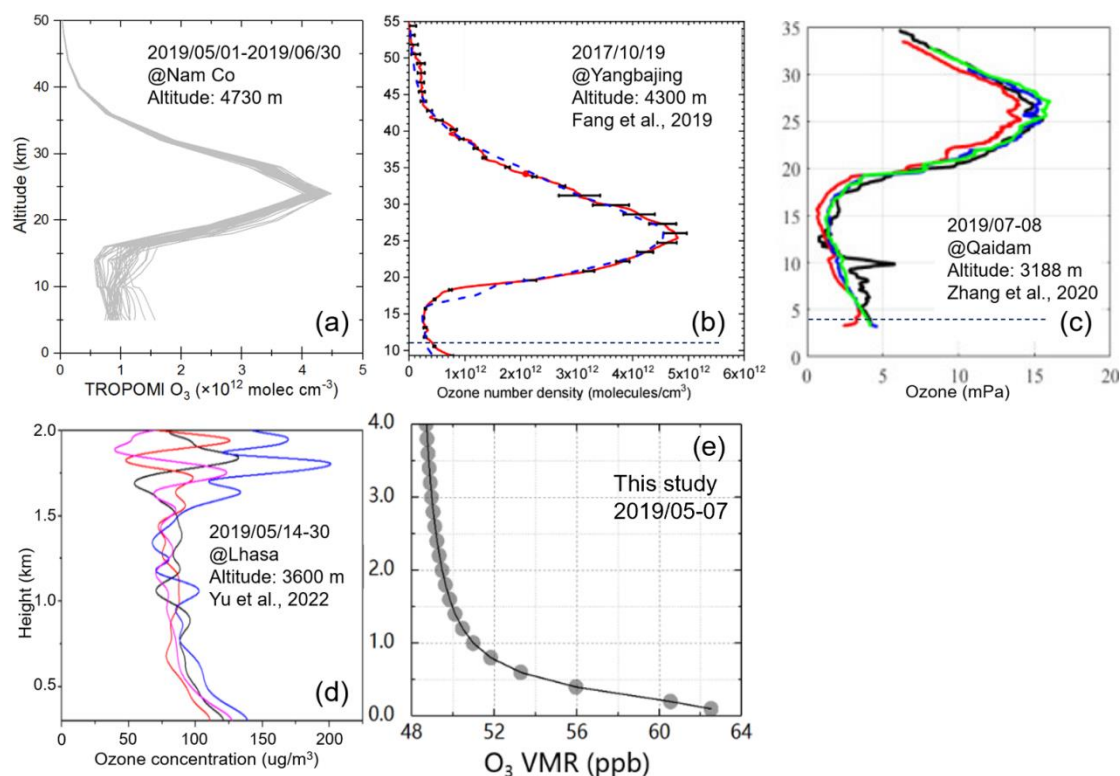

Figure R13. Ozone vertical profile measure by (a) TROPOMI at Nam Co, (b) lidar at Yangbajing (Fang et al., 2019), (c) ozonesonde at Qaidam (Zhang et al., 2020), (d) lidar at Lhasa (Yu et al., 2022), and (e) MAX-DOAS in this study.

16. Line 251: Please add "O_3".
Re: Thanks for your great comments. We have modified it as "3.2 Vertical distributions of aerosol, H_2O, NO_2, HONO and O_3"

17. Line 254-255: Why are NO_2 vertical profiles "Gaussian" distribution rather than Lorentz or other peak distribution?
Re: Thanks for your great comments.
As shown in Figure R2 (a), the aerosol vertical profile retrieved from MAX-DOAS show the best agreement with lidar measurement result. However, lidar could more accurately characterize the thickness of the layer of aerosol with high values. It should be attributed to lidar having a higher vertical resolution than MAX-DOAS. The vertical resolution of MAX-DOAS and lidar are 100 m and 7.5 m, respectively. Due to the uncertainty of the algorithm, MAX-DOAS is more insensitive at high altitudes and the degrees of freedom is often only 3 to 5. It is similar to the retrieval of NO_2 vertical profile. *Therefore, in addition to the true vertical distribution of NO_2, the factors limiting the shape of NO_2 vertical profile also include the limited vertical resolution*

and the low degree of freedom of the vertical profiles. The NO_2 profile showed a Gaussian shape during our observation.

Referred to our previous study (Xing et al., 2017), we defined a Lorentz a priori with equivalent aerosol loading compared to the corresponding lidar profile. We found that the aerosol profile retrieved from Lorentz a priori shows a significant overestimation compared to the lidar results between 1 and 2 km. Besides, the degree of freedom of signal (DFS) of using Gaussian a priori (2.96) is higher than that of using Lorentz a priori (2.4). The retrieved error of adopting Lorentz a priori is relatively higher than the Gaussian a priori at the lowest 1 km (see Figure R14). This also goes some way to proof of rationality of MAX-DOAS Gaussian profile compared to the Lorentz profile.
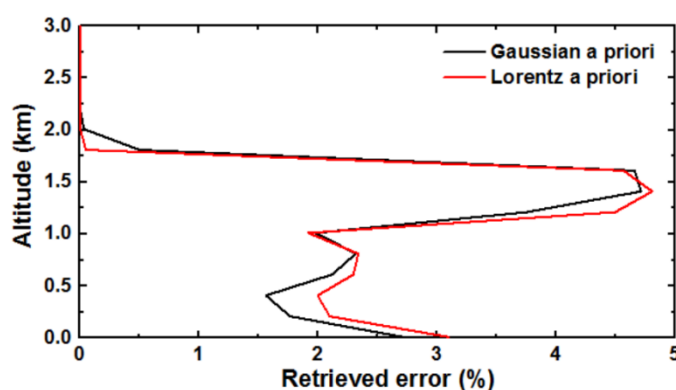
Figure R14. The retrieved error of using Gaussian and Lorentz a priori for aerosol retrieval.

18. Line 264-265: Please clarify the monsoon transport leading to the elevation of maximum H_2O layer.

Re: Thanks for your great comments.

As shown in Figure R15, we could find the Indian monsoon gradually increased from June, the stronger monsoon lasted from early June until the end of September. But we could find that there was a significantly decrease for the Indian monsoon index in the early July. Our campaign was from 01 May to 09 July 2019. It could explain the elevation of the height layers of maximum water vapor in June.
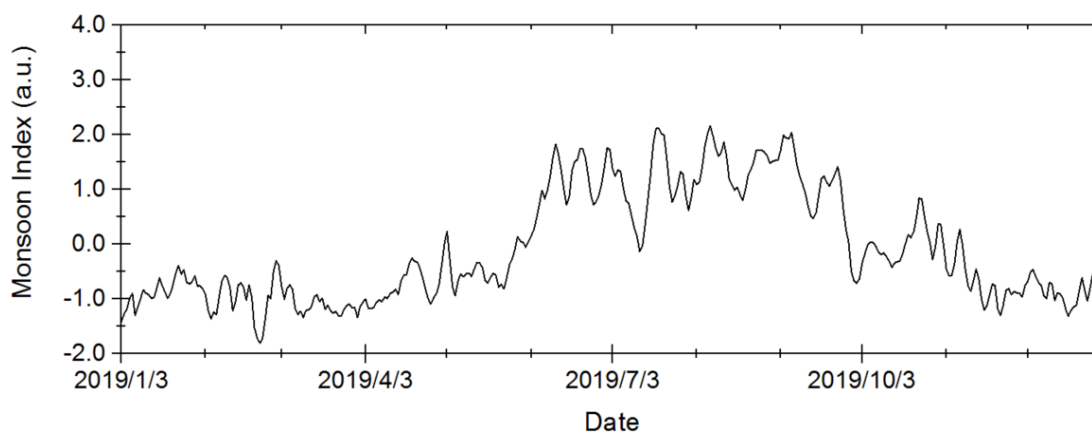
Figure R15. The Indian monsoon index during 2019.

Moreover, we have rewritten this sentence as "*The monthly averaged vertical profile of*

H$_2$O in May and July exhibited an exponential shape, while its maximum concentration layer slightly elevated to 0.1-0.2 km in June which was related to the strongest monsoon transport.".

19. Line 279-282: With respect to the vertical profiles of atmospheric component at the height of 3-4 km, are the retrieved data valid? How to understand the differences of O$_3$ profiles between "exponential shape" (Line 282) and "relatively uniform vertical gradient" (Line 240)?

Re: Thanks for your great comments.

The averaging kernels at higher altitudes (> 2.0 km) were relatively lower than that at low altitudes. This could lead to a reduction in the sensitivity of pollutants' concentrations at high altitudes. The uncertainty of the concentrations of pollutants at high altitudes were also larger than that at lower altitudes. However, this did not mean that the profiles at 3-4 km were not credible. Several previous studies also carried out scientific research using MAX-DOAS profiles with a height range of 0.0-4.0 km (Wang et al., 2019; Hoque et al., 2022; Kuhn et al., 2024). The vertical profiles of aerosol and trace gases (0.0-4.0 km) retrieved from MAX-DOAS were validated with aircraft measurements and model simulations, and they all shown good agreement (Wang et al., 2019; Hoque et al., 2022; Kuhn et al., 2024). It indicated that the MAX-DOAS profiles at high altitude were credible. For O$_3$ vertical profile, since we used the TROPOMI O$_3$ profiles as a constraint, its sensitivity was stronger above 3km. In this study, we only validated the surface concentrations of pollutants during our measurements, considering the absence of other independent vertical observations. We focused on analyzing concentration variations of pollutants below the PBL.

There may be a misunderstanding like comment 12. Figure 4 depicted the time series of daily averaged concentrations of pollutants at five altitudes during the whole observations. Figure 5 showed the averaged diurnal variations pollutants. As shown in Figure 4, we could find that the ratios of O$_3$ at 0.4-0.6 km, 0.8-1.0 km, 1.2-1.4 km and 1.6-1.8 km to those at 0.0-0.2 km were 89.25%, 82.44%, 80.16% and 79.13%, respectively. Therefore, we concluded that the vertical gradient of daily averaged O$_3$ concentration was also not obvious. We have rewritten this sentence as "The vertical gradient of daily averaged O$_3$ concentration was also not obvious, which was associated with its vertical mixing and photochemical production".

20. Line 298-301: It just lists the possible influencing factors here. To what extent, can the weak surface wind affect the sand-raising process?

Re: Thanks for your great comments.

The diurnal variation showed a bi-peak pattern, which was in line with the investigation reported by Pokharel et al. (2019). The first peak should be attributed to the local emission of aerosol and the diurnal cycle of PBL (Zhang et al., 2017; Pokharel et al., 2019). The second peak was driven by regional transport and the interaction between local sandy silt loam surface and local meteorology. Figure R4 told us that the high wind speed (> 4.5 m/s) at surface appeared after 15:00, which coincided with the appearance of the second aerosol peak. As shown in Figure 5, the high extinction during

the second peak period was extended to 1.0 km. Figure R16 told us that the wind speed above 500 m was larger than 8 m/s, which created a favorable condition for high-altitude aerosol transport.

In addition, we also noticed that there would be drift blown up by the wind at the measurement site after 15:00 during the whole observation period.
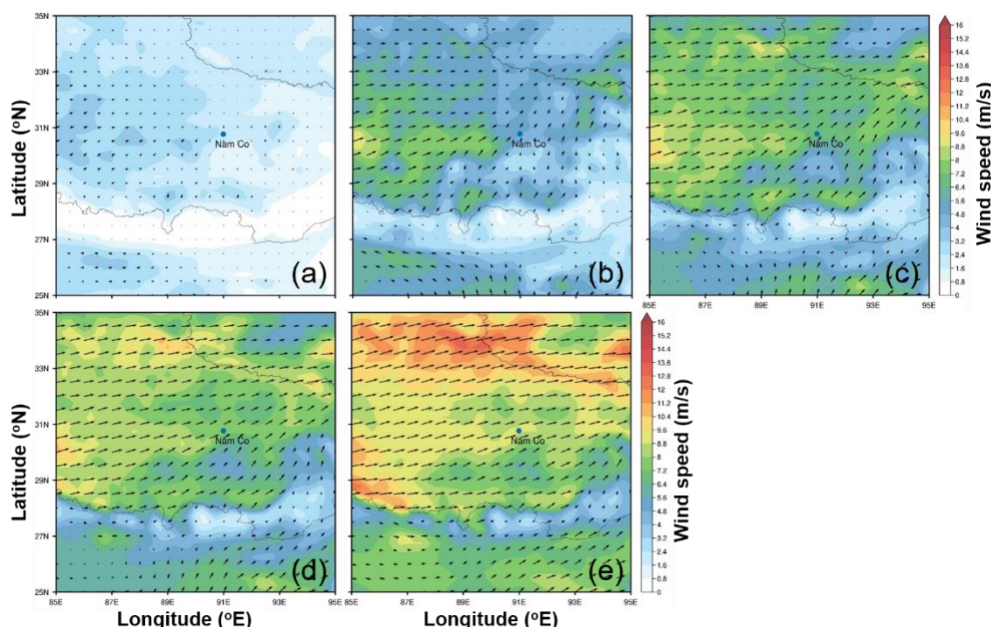

Figure R16. Wind direction and wind speed at (a) 10 m, (b) 500 m, (c) 1000 m, (d) 1300 m, and (e) 1800 m at a range of 25°N-35°N and 85°E-95°E, respectively.

These sentences have been rewritten as "*The first peak should be attributed to the local emission of aerosol and the diurnal cycle of PBL (Zhang et al., 2017; Pokharel et al., 2019). The second peak was driven by regional transport and the interaction between local sandy silt loam surface and local meteorology. The high wind speed (> 4.5 m/s) at surface appeared after 15:00, which coincided with the appearance of the second aerosol peak (Figure S3). Moreover, the high extinction during the second peak was extended to 1.0 km associated with the wind speed larger than 8 m/s (Figure S7), which created a favorable condition for high-altitude aerosol transport.*".

21. Line 302-308: Please check the attribution of H_2O and NO_2 variations. For example, the monsoon not only affect the H_2O variation in the morning but also in the afternoon.
Re: Thanks for your great comments.
We couldn't agree with you more. There maybe some misunderstandings for the sentences of "*The first peak appeared between 08:00-12:00, which was mainly affected by the monsoon drived long-range transport of H_2O. The second and third peaks occurred at 15:00-16:00 and after 17:00, respectively. In addition to long-range transport, the enhanced evaporation from the Nam Co lake also significantly contributed to the appearance of these two peaks of H_2O.*". It means that these three peaks of H_2O all affected by the monsoon drived long-range transport. In addition, the enhanced evaporation from the Nam Co lake also significantly contributed to the second and third H_2O peaks.

For the source of NO_2, we have rewritten the corresponding sentences as "*NO_2 mainly distributed at 0.2-0.4 km, and peaked before 10:00 and after 18:00 which were dominated by the effects of local emissions and regional transport from the NOx formed through ice and snow on the top of Mt. Tanggula under strong ultraviolet radiation (Figure S5) (Boxe et al., 2005; Fisher 2005; Chen et al., 2019; Lin et al., 2021).*". Detailed analysis could referred to comment 12.

22. Line 314-315: Please check that the text description is consistent with the figures.
Re: Thanks for your great comments.
We confirmed that the text description is consistent with Figure 5. In order to determine this fact, we analyzed the averaged aerosol, H_2O, NO_2 and HONO profiles during three HONO peak periods (Figure R17).

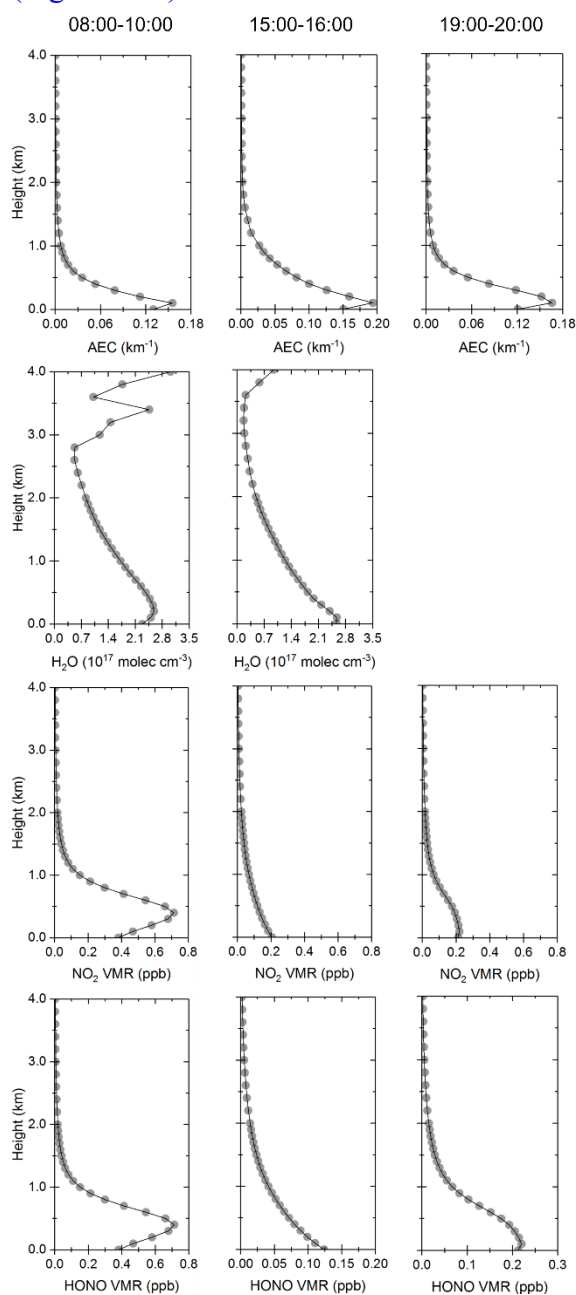Figure R17. The averaged aerosol, H_2O, NO_2 and HONO profiles during three HONO

peak periods

23. Figure 7: The validity of results above 3 km should be carefully checked. Probably the concentrations of atmospheric component at higher height mainly reflected a priori information.

Re: Thanks for your great comments.

The averaging kernels at higher altitudes (> 2.0 km) were relatively lower than that at low altitudes. This could lead to a reduction in the sensitivity of pollutants' concentrations at high altitudes. The uncertainty of the concentrations of pollutants at high altitudes were also larger than that at lower altitudes. However, this did not mean that the profiles at 2-4 km were not credible. Several previous studies also carried out scientific research using MAX-DOAS profiles with a height range of 0.0-4.0 km (Wang et al., 2019; Hoque et al., 2022; Kuhn et al., 2024). The vertical profiles of aerosol and trace gases (0.0-4.0 km) retrieved from MAX-DOAS were validated with aircraft measurements and model simulations, and they all shown good agreement (Wang et al., 2019; Hoque et al., 2022; Kuhn et al., 2024). It indicated that the MAX-DOAS profiles at high altitude were credible. For O_3 vertical profile, since we used the TROPOMI O_3 profiles as a constraint, its sensitivity was stronger above 2 km. In this study, we only validated the surface concentrations of pollutants during our measurements, considering the absence of other independent vertical observations. We focused on analyzing concentration variations of pollutants below the PBL.

24. Line 388-390: Is that so?

Re: Thanks for your great comments.

This is our mistake. We added dashed line representing the scatter distribution envelope in Figure R18. We could find that the maximum value of $HONO/NO_2$ appeared around water vapor being around 1.0×10^{17} molec cm^{-3} under 1.0 km, and being around 1.0-2.0×10^{17} molec cm^{-3} at 0.5-1.0 km height layer.
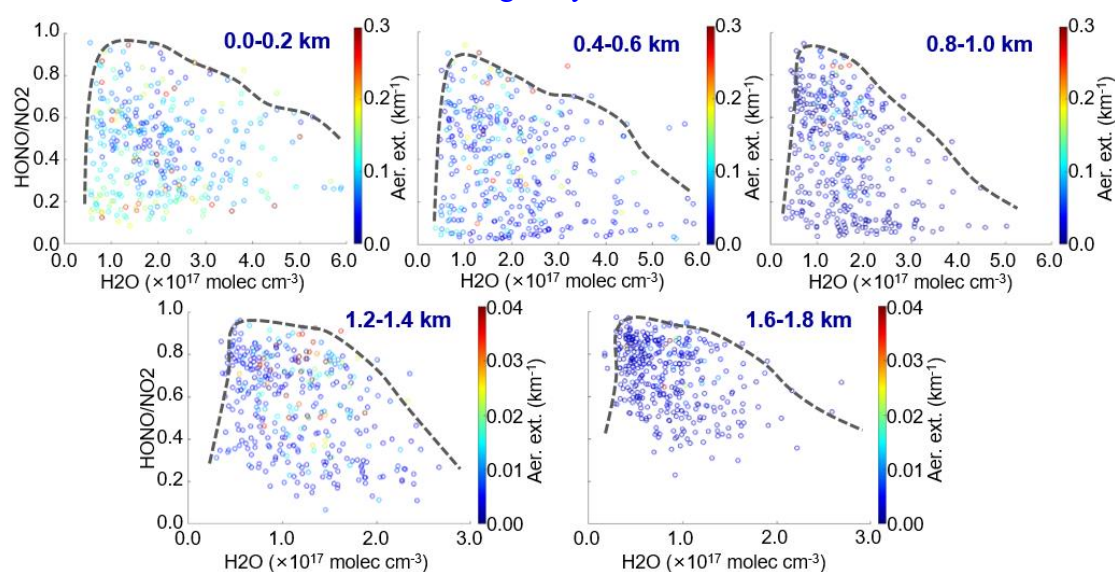

Figure R18. Scatter plots between $HONO/NO_2$ and H_2O colored by aerosol extinction at (a) 0.0-0.2 km, (b) 0.4-0.6 km, (c) 0.8-1.0 km, (d) 1.2-1.4 km, (and e) 1.6-1.8 km

from 1st May to 9th July 2019. The dashed line represents the scatter distribution envelope.

This sentence has been modified as "*We found that the maximum value of HONO/NO$_2$ appeared around water vapor being around 1.0×10^{17} molec cm^{-3} under 1.0 km, and being around $0.5\text{-}1.0\times10^{17}$ molec cm^{-3} at 1.0-2.0 km height layer.*".

25. Figure 9: Please add the graphic symbol description, such as error bar. Please modify all the similar problems in other figures.

Re: Thanks for your great comments. We have made following modifications.

(1) Figure 9. Statistics for the vertical profile of HONO/NO$_2$ from 1st May to 9th July 2019. The left and right of the blue box represent the 25th and 75th percentiles, respectively; the dot within the box represent the mean.

(2) Figure 3. Averaged diurnal variation of AOD at CAS (NAMORS). The error bars represent the mean retrieved errors of AOD.

(3) Figure 6. Validations of (a) MAX-DOAS NO$_2$ vs in situ NO$_2$ (error bars represent the retrieved errors of NO$_2$ from MAX-DOAS and BBCES), (b) MAX-DOAS HONO vs LOPAP HONO, (c) MAX-DOAS O$_3$ vs in situ O$_3$, and (d) MAX-DOAS PBL vs WRF PBL.

26. Line 420: three clusters? There are four clusters in Figure S7e.

Re: Thanks for your great comments. We have made modifications as following:

"*As shown in Figure S9 and Table 4, the backward trajectories arriving at NAMORS during the observation were classified into three clusters at 200 m, 600 m, 1400 m, 1800 m, and four clusters at 1000 m. We found that cluster 3 was associated with the highest O$_3$ concentration at 200 m (65.48±17.41 ppb) and 1800 m (49.69±2.21 ppb), and cluster 1 were related to the highest O3 concentration at 600 m (54.67±6.94 ppb), 1000 m (51.61±3.84 ppb) and 1400 m (50.51±2.89 ppb).*"

Table 4. Trajectory ratios and averaged O$_3$ concentration for all trajectory clusters arriving in Nam Co at 200 m, 600 m, 1000 m, 1400 m and 1800 m from May to July 2019.

| | Cluster | Traj_ratio | O$_3$ concentration (ppb) |
			Mean ±SD
200 m	1	55.86%	61.50 ±18.15
	2	11.85%	54.57 ±14.67
	3	32.28%	65.48 ±17.41
	All	100.00%	61.14 ±17.74
600 m	1	62.55%	54.67 ±6.94
	2	14.32%	50.43 ±6.64
	3	23.13%	53.27 ±7.63
	All	100.00%	53.39 ±7.26
1000 m	1	49.16%	51.61 ±3.84
	2	8.81%	49.60 ±3.99
	3	22.73%	50.72 ±4.21
	4	19.30%	51.39 ±4.49

	All	100.00%	50.98 ±4.30
1400 m	1	80.14%	50.51 ±2.89
	2	4.95%	49.12 ±2.73
	3	14.92%	49.44 ±3.85
	All	100.00%	50.07 ±3.15
1800 m	1	83.75%	49.68 ±2.55
	2	0.00%	49.07 ±2.23
	3	16.25%	49.69 ±2.21
	All	100.00%	49.59 ±2.49

27. Line 434-437: The discussion of stratospheric O_3 intrusion is too simple. The logic is confusing between stratosphere intrusion and long-range transport.

Re: Thanks for your great comments.

Several previous studies have revealed that the stratospheric O_3 intrusion events were frequent in the Himalayas during spring and summer. The O_3 from stratospheric intrusions in the Himalayas can affect the O_3 at NAMORS through long-range transport. Figure R19 showed that the contribution of O_3 transported from Himalayas can even up to 50 ppb, especially under 600 m.
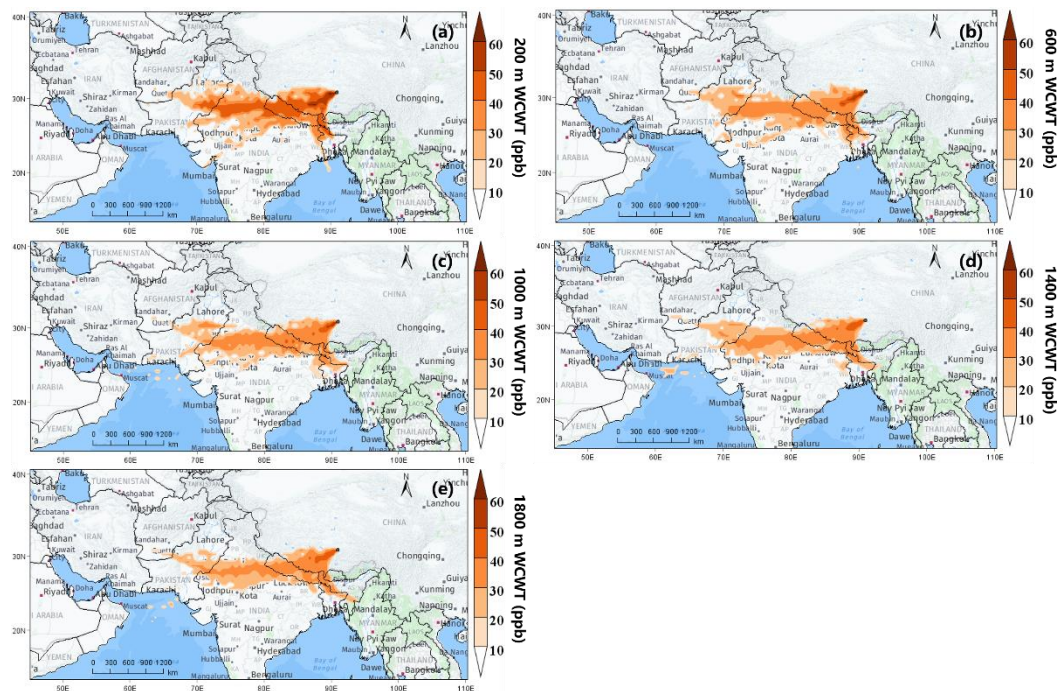

Figure R19. Spatial distributions of WCWT values for O_3 at (a) 200 m, (b) 600 m, (c) 1000 m, (d) 1400 m, and (e) 1800 m height layers from 01st May to 09th July 2019 over CAS (NAMORS).

We can understand the process as following:

The WCWT showed that the Himalayas was a very important potential source area of O_3 at NAMORS. Therefore, we should also understand the source of O_3 in the Himalayas. Several previous studies have revealed that the stratospheric O_3 intrusions were an important source of O_3 in the Himalayas during spring and summer.

Theses sentences have been modified as "*In addition, Figure 10 showed that the*

contribution of O₃ transported from Himalayas can even up to 50 ppb, especially under 600 m. Several previous studies have revealed that the stratospheric O₃ intrusion events were frequent in the Himalayas during spring and summer (Cristofanelli et al., 2010; Chen et al., 2011; Škerlak et al., 2014; Putero et al., 2016). Therefore, the O₃ from stratospheric intrusions in the Himalayas can affect the O₃ at NAMORS through long-range transport.".

It should be noted that our present observational data do not capture the O₃ stratospheric intrusion process in the Himalaya. We also hope to follow this work in the future.

28. Section References (Line 482-854): Although there are too many references, the key references related to this topic are missing.

Re: Thanks for your great comments.

We have added some literature that supports our some conclusions in the study.

Added references:

[1] Fisher, F. N.: Extinction of UV-visible radiation in wet midlatitude (maritime) snow: Implications for increased NOx emission, J. Geophys. Res., 110, D21301, doi:10.1029/2005JD005963, 2005.

[2] Lin, W., Wang, F., Ye, C., Zhu, T.: Observation of strong NO_x release over Qiyi Glacier, China. The Cryosphere, doi.org/10.5194/tc-2021-32, 2021.

[3] Ji, X., Liu, C., Wang, Y., Hu, Q., Lin, H., Zhao, F., Xing, C., Tang, G., Zhang, J., Wagner, T.: Ozone profiles without blind area retrieved from MAX-DOAS measurements and comprehensive validation with multi-platform observations. Remote Sens. Environ., 284, 113339, doi.org/10.1016/j.res.2022.113339, 2023.

[4] Lin, H., Liu, C., Xing, C., Hu, Q., Hong, Q., Liu, H., Li, Q., Tan, W., Ji, X., Wang, Z., Liu, J.: Validation of water vapor vertical distributions retrieved from MAX-DOAS over Beijing, China. Remote Sens., 12, 3193, doi.org/10.3390/rs12193193, 2020.

[5] Xing, C., Xu, S., Song, Y., Liu, C., Liu, Y., Lu, K., Tan, W., Zhang, C., Hu, Q., Wang, S., Wu, H., Lin, H.: A new insight into the vertical differences in NO_2 heterogeneous reaction to produce HONO over inland and marginal seas. Atmos. Chem. Phys., 23, 5815-5834, doi.org/10.5194/acp-23-5815-2023, 2023.

[6] Rodgers, C. D.: Inverse methods for atmospheric sounding: theory and practice. Singapore-New Jersey-London-Hong: World Scientific Publishing; 2000.

[7] Wagner, T., Dix, B., FriedeBurg, C. V., Frieß, U., Sanghavi, S., Sinreich, R., Platt, U.: MAX-DOAS O_4 measurements: A new technique to derive information on atmospheric aerosols-Principles and information content. J. Geophys. Res.: Atmos., 109, D22205, doi.org/10.1029/2004jd004904, 2004.

[8] Serdyuchenko, A., Gorshelev, V., Weber, M., Chehade, W., Burrows, J. P.: High spectral resolution ozone absorption cross-sections-Part 2: Temperature dependence. Atmos. Meas. Tech., 7, 625-636, doi:10.5194/amt-7-625-2014, 2014.

[9] Wang, Y., Lampel, J., Xie, P., Beirle, S., Li, A., Wu, D., Wagner, T.: Ground-based MAX-DOAS observations of tropospheric aerosols, NO_2, SO_2 and HCHO in Wuxi, China, from 2011 to 2014. Atmos. Chem. Phys., 17, 2189-2215, doi.org/10.5194/acp-17-2189-2017, 2017.

[10] Wang, Y., Apituley, A., Bais, A., Beirle, S., Benavent, N., Borovski, A., Bruchkouski, I., Chan, K. L., Donner, S., Drosoglou, T., Finkenzeller, H., Friedrich, M.

M., Frieß, U., Garcia-Nieto, D., Gómez-Martín, L., Hendrick, F., Hilboll, A., Jin, J., Johnston, P., Koenig, T. K., Kreher, K., Kumar, V., Kyuberis, A., Lampel, J., Liu, C., Liu, H., Ma, J., Polyansky, O. L., Postylyakov, O., Querel, R., Saiz-Lopez, A., Schmitt, S., Tian, X., Tirpitz, J. L., Van Roozendeal, M., Volkamer, R., Wang, Z., Xie, P., Xing, C., Xu, J., Yela, M., Zhang, C., Wagner, T.: Inter-comparison of MAX-DOAS measurements of tropospheric HONO slant column densities and vertical profiles during the CINDI-2 campaign. Atmos. Meas. Tech., 13, 5087–5116, doi.org/10.5194/amt-13-5087-2020, 2020.

[11] Thalman, R., Volkamer, R.: Temperature dependent absorption cross-sections of O_2-O_2 collision pairs between 340 and 630 nm and at atmospherically relevant pressure. Phys. Chem. Chem. Phys., 15, 15371-15381, doi:10.1039/C3CP50968K, 2013.

[141] Vandaele, A. C., Hermans, C., Simon, P. C., Carleer, M., Colin, R., Fally, S., Merienne, M. F., Jenouvrier, A., Coquart, D.: Measurements of the NO_2 absorption cross-section from 42000 cm^{-1} to 10000 cm^{-1} (238–1000nm) at 220K and 294K. J. Quant. Spectrosc. Ra., 59, 171-184, doi:10.1016/S0022-4073(97)00168-4, 1998.

[12] Stutz, J., Kim, E. S., Platt, U., Bruno, P., Perrino, C., Febo, A.: UV-visible absorption cross sections of nitrous acid. J. Geophys. Res.: Atmos., 105, 14585-14592, doi:10.1029/2000JD900003, 2000.

[13] Aliwell, S. R., Van Roozendael, M., Johnston, P. V., Richter, A., Wagner, T., Arlander, D. W., Burrows, J. P., Fish, D. J., Jones, R. L., Tørnkvist, K. K., Lambert, J. C., Pfeilsticker, K., and Pundt, I.: Analysis for BrO in zenith-sky spectra: an intercomparison exercise for analysis improvement, J. Geophys. Res., 107, ACH 10-1–ACH 10-20, https://doi.org/10.1029/2001JD000329, 2002.

[14] Vandaele, A. C., Hermans, C., Simon, P. C., Carleer, M., Colin, R., Fally, S., Mérienne, M. F., Jenouvrier, A., and Coquart, B.: Measurements of the NO_2 absorption cross section from 42000 cm^{-1} to 10000 cm^{-1} (238–1000nm) at 220 K and 294 K, J. Quant. Spectrosc. Ra., 59, 171–184, doi:10.1016/S0022-4073(97)00168, 1998.

[15] Meller, R. and Moortgat, G. K.: Temperature dependence of the absorption cross sections of formaldehyde between 223 and 323 K in the wavelength range 225–375nm, J. Geophys. Res., 105, 7089–7101, doi:10.1029/1999JD901074, 2000.

[16] Volkamer, R., Spietz, P., Burrows, J., Platt, U.: High-resolution absorption cross-section of glyoxal in the UV-vis and IR spectral ranges, J. Photochem. Photobiol. A Chem., 172, 35–46, doi:10.1016/j.jphotochem.2004.11.011, 2005.

[17] Rothman, L. S., Gordon, I. E., Barbe, A., Benner, D. C., Bernath, P. E., Birk, M., Boudon, V., Brown, L. R., Campargue, A., Champion, J. P., Chance, K., Coudert, L. H., Dana, V., Devi, V. M., Fally, S., Flaud, J. M., Gamache, R. R., Goldman, A., Jacquemart, D., Kleiner, I., Lacome, N., Lafferty, W. J., Mandin, J. Y., Massie, S. T., Mikhailenko, S. N., Miller, C. E., Moazzen-Ahmadi, N., Naumenko, O. V., Nikitin, A. V., Orphal, J., Perevalov, V. I., Perrin, A., Predoi-Cross, A., Rinsland, C. P., Rotger, M., Simeckova, M., Smith, M. A. H., Sung, K., Tashkun, S. A., Tennyson, J., Toth, R. A., Vandaele, A. C., Vander Auwera, J.: The HITRAN 2008 molecular spectroscopic database, J. Quant. Spectrosc. Radiat. Transf., 110, 533–572, 2009.

[18] Fleischmann, O. C., Hartmann, M., Burrows, J. P., and Orphal, J.: New ultraviolet absorption cross-sections of BrO at atmospheric temperatures measured by time-

windowing Fourier transform spectroscopy, J. Photoch. Photobio. A, 168, 117–132, 2004.

[19] Ward Jr, J. H.: Hierarchical grouping to optimize an objective function, J. Am. Stat. Assoc., 58, 236-244, 1963.

[20] Wang, Y., Zhang, X., Arimoto, R.: The contribution from distant dust sources to the atmospheric particulate matter loading at XiAn, China during spring, Sci. Total Environ., 368, 875-883, 2006.

[21] Cheng, S., Pu, G., Ma, J., Hong, H., Du, J., Yudron, T., Wagner, T.: Retrieval of tropospheric NO_2 vertical column densities from ground-based MAX-DOAS measurements in Lhasa, a city on the Tibetan Plateau, Remote Sens., 15, 4689, 2023a.

[22] Cheng, S., Ma, J., Zheng, A., Gu, M., Donner, S., Donner, S., Zhang, W., Du, J., Li, X., Liang, Z., Lv, J., Wagner, T.: Retrieval of O_3, NO_2, BrO and OClO columns from ground-based zenith scattered light DOAS measurements in summer and autumn over the Northern Tibetan Plateau, Remote Sens., 13, 4242, 2021.

[23] Ma, J., Donner, S., Donner, S., Jin, J., Cheng, S., Guo, J., Zhang, Z., Wang, J., Liu, P., Zhang, G., Pukite, J., Lampel, J., Wagner, T.: MAX-DOAS measurements of NO_2, SO_2, HCHO, and BrO at the Mt. Waliguan WMO GAW global baseline station in the Tibetan Plateau, Atmos. Chem. Phys., 20, 6973-6990, 2020.

[24] Cheng, S., Cheng, X., Ma, J., Xu, X., Zhang, W., Lv, J., Bai, G., Chen, B., Ma, S., Ziegler, S., Donner, S., Wagner, T.: Mobile MAX-DOAS observations of tropospheric NO_2 and HCHO during summer over the Three Rivers' Source region in China, Atmos. Chem. Phys., 23, 3655-3677, 2023b.

[25] Li, M., Mao, J., Chen, S., Bian, J., Bai, Z., Wang, X., Chen, W., Yu, P.: Significant contribution of lightning NO_x to summertime surface O_3 on the Tibetan Plateau, Sci. Total Environ., 829, 154639, 2022.

In addition, most of the current work on atmospheric monitoring on the TP, especially vertical monitoring, was carried out by Chinese scholars.

References

[1] Ward Jr, J. H.: Hierarchical grouping to optimize an objective function, J. Am. Stat. Assoc., 58, 236-244, 1963.

[2] Wang, Y., Zhang, X., Arimoto, R.: The contribution from distant dust sources to the atmospheric particulate matter loading at XiAn, China during spring, Sci. Total Environ., 368, 875-883, 2006.

[3] Aliwell, S. R., Van Roozendael, M., Johnston, P. V., Richter, A., Wagner, T., Arlander, D. W., Burrows, J. P., Fish, D. J., Jones, R. L., Tørnkvist, K. K., Lambert, J. C., Pfeilsticker, K., and Pundt, I.: Analysis for BrO in zenith-sky spectra: an intercomparison exercise for analysis improvement, J. Geophys. Res., 107, ACH 10-1–ACH 10-20, https://doi.org/10.1029/2001JD000329, 2002.

[4] Vandaele, A. C., Hermans, C., Simon, P. C., Carleer, M., Colin, R., Fally, S., Mérienne, M. F., Jenouvrier, A., and Coquart, B.: Measurements of the NO_2 absorption cross section from 42000 cm^{-1} to 10000 cm^{-1} (238–1000nm) at 220 K and 294 K, J. Quant. Spectrosc. Ra., 59, 171–184, 1998.

[5] Meller, R. and Moortgat, G. K.: Temperature dependence of the absorption cross sections of formaldehyde between 223 and 323 K in the wavelength range 225–375 nm, J. Geophys. Res., 105, 7089–7101, 2000.

[6] Volkamer, R., Spietz, P., Burrows, J., Platt, U.: High-resolution absorption cross-section of glyoxal in the UV-vis and IR spectral ranges, J. Photochem. Photobiol. A Chem., 172, 35–46, 2005.

[7] Rothman, L. S., Gordon, I. E., Barbe, A., Benner, D. C., Bernath, P. E., Birk, M., Boudon, V., Brown, L. R., Campargue, A., Champion, J. P., Chance, K., Coudert, L. H., Dana, V., Devi, V. M., Fally, S., Flaud, J. M., Gamache, R. R., Goldman, A., Jacquemart, D., Kleiner, I., Lacome, N., Lafferty, W. J., Mandin, J. Y., Massie, S. T., Mikhailenko, S. N., Miller, C. E., Moazzen-Ahmadi, N., Naumenko, O. V., Nikitin, A. V., Orphal, J., Perevalov, V. I., Perrin, A., Predoi-Cross, A., Rinsland, C. P., Rotger, M., Simeckova, M., Smith, M. A. H., Sung, K., Tashkun, S. A., Tennyson, J., Toth, R. A., Vandaele, A. C., Vander Auwera, J.: The HITRAN 2008 molecular spectroscopic database, J. Quant. Spectrosc. Radiat. Transf., 110, 533–572, 2009.

[8] Fleischmann, O. C., Hartmann, M., Burrows, J. P., and Orphal, J.: New ultraviolet absorption cross-sections of BrO at atmospheric temperatures measured by time-windowing Fourier transform spectroscopy, J. Photoch. Photobio. A, 168, 117–132, 2004.

[9] Cheng, S., Pu, G., Ma, J., Hong, H., Du, J., Yudron, T., Wagner, T.: Retrieval of tropospheric NO_2 vertical column densities from ground-based MAX-DOAS measurements in Lhasa, a city on the Tibetan Plateau, Remote Sens., 15, 4689, 2023.

[10] Cheng, S., Ma, J., Zheng, A., Gu, M., Donner, S., Donner, S., Zhang, W., Du, J., Li, X., Liang, Z., Lv, J., Wagner, T.: Retrieval of O_3, NO_2, BrO and OClO columns from ground-based zenith scattered light DOAS measurements in summer and autumn over the Northern Tibetan Plateau, Remote Sens., 13, 4242, 2021.

[11] Ma, J., Donner, S., Donner, S., Jin, J., Cheng, S., Guo, J., Zhang, Z., Wang, J., Liu, P., Zhang, G., Pukite, J., Lampel, J., Wagner, T.: MAX-DOAS measurements of NO_2, SO_2, HCHO, and BrO at the Mt. Waliguan WMO GAW global baseline station in the

Tibetan Plateau, Atmos. Chem. Phys., 20, 6973-6990, 2020.

[12] Cheng, S., Cheng, X., Ma, J., Xu, X., Zhang, W., Lv, J., Bai, G., Chen, B., Ma, S., Ziegler, S., Donner, S., Wagner, T.: Mobile MAX-DOAS observations of tropospheric NO_2 and HCHO during summer over the Three Rivers' Source region in China, Atmos. Chem. Phys., 23, 3655-3677, 2023.

[13] Xing, C., Liu, C., Wu, H., Lin, J., Wang, F., Wang, S., Gao, M.: Ground-based vertical profile observations of atmospheric composition on the Tibetan Plateau (2017-2019), Earth Syst. Sci. Data, 13, 4897-4912, 2021.

[14] Li, M., Mao, J., Chen, S., Bian, J., Bai, Z., Wang, X., Chen, W., Yu, P.: Significant contribution of lightning NO_x to summertime surface O_3 on the Tibetan Plateau, Sci. Total Environ., 829, 154639, 2022.

[15] Xing, C., Liu, C., Wang, S., Chan, K. L., Gao, Y., Huang, X., Su, W., Zhang, C., Dong, Y., Fan, G., Zhang, T., Chen, Z., Hu, Q., Su, H., Xie, Z., Liu, J.: Observations of the vertical distributions of summertime atmospheric pollutants and the corresponding ozone production in Shanghai, China, Atmos. Chem. Phys., 17, 14275-14289, doi:10.5194/acp-17-14275-2017, 2017.

[16] Ji, X., Liu, C., Wang, Y., Hu, Q., Lin, H., Zhao, F., Xing, C., Tang, G., Zhang, J., Wagner, T.: Ozone profiles without blind area retrieved from MAX-DOAS measurements and comprehensive validation with multi-platform observations, Remote Sens. Environ., 284, 113339, doi:10.1016/j.rse.2022.113339, 2022.

[17] Fisher F N. Extinction of UV-visible radiation in wet midlatitude (maritime) snow: Implications for increased NO_x emission. Journal of Geophysical Research, 110, D21301, doi:10.1029/2005JD005963, 2005.

[18] Lin W, Wang F, Ye C, Zhu T. Observation of strong NO_x release over Qiyi Glacier, China. The Cryosphere, doi.org/10.5194/tc-2021-32, 2021.

[19] Fang, X., Li, T., Ban, C., Wu, Z., Li, J., Li, F., Cen, Y., and Tian, B.: A mobile differential absorption lidar for simultaneous observations of tropospheric and stratospheric ozone over Tibet, Opt. Express, 2019, 27(4), 4126-4139, doi:10.1364/OE.27.004126.

[20] Yu, J., Meng, L., Chen, Y., Zhang, H., and Liu, J.: Ozone profiles, precursors, and vertical distribution in urban Lhasa, Tibetan Plateau, Remote Sens., 2022, 14(11), doi:10.3390/rs14112533.

[21] Zhang, J., Xia, X., and Wu, X.: First in situ UV profile across the UTLS accompanied by ozone measurement over the Tibetan Plateau, J. Environ. Sci., 2020, 98, 71-76, doi:10.1016/j.jes.2020.05.020.

[22] Kuhn, L., Beirle, S., Kumar, V., Osipov, S., Pozzer, A., Bosch, T., Kumar, R., Wagner, T.: On the influence of vertical mixing, boundary layer schemes, and temporal emission profiles on tropospheric NO_2 in WRF-Chem-comparisons to in situ, satellite, and MAX-DOAS observations, Atmos. Chem. Phys., 2024, 24, 185-217, doi:10.5194/acp-24-185-2024.

[23] Hoque, H. M. S., Sudo, K., Irie, H., Damiani, A., Naja, M., Fatmi, A. M.: Multi-axis differential optical absorption spectroscopy (MAX-DOAS) observations of formaldehyde and nitrogen dioxide at three sites in Asia and comparison with the global chemistry transport model CHASER, Atmos. Chem. Phys., 2022, 22, 12559-12589,

doi:10.5194/acp-22-12559-2022.

[24] Wang, Y., Donner, S., Donner, S., Bohnke, S., De Smedt, I., Dickerson, R. R., Dong, Z., He, H., Li, Z., Li, Z., Li, D., Liu, D., Ren, X., Theys, N., Wang, Y., Wang, Y., Wang, Z., Xu, H., Xu, J., Wagner, T.: Vertical profiles of NO_2, SO_2, HONO, HCHO, CHOCHO and aerosols derived from MAX-DOAS measurements at a rural site in the central western North China Plain and their relation to emission sources and effects of regional transport, Atmos. Chem. Phys., 2019, 19, 5417-5449, doi:10.5194/acp-19-5417-2019.

[25] Pokharel, M., Guang, J., Liu, B., Kang, S., Ma, Y., Holben, B.N., Xia, X., Xin, J., Ram, K., Rupakheti, D., Wan, X., Wu, G., Bhattarai, H., Zhao, C., and Cong, Z.: Aerosol properties over Tibetan Plateau from a decade of AERONET measurements: Baseline, types, and influencing factors, J. Geophys. Res.: Atmos., 124, 13357-13374, doi:10.1029/2019JD031293, 2019.

[26] Wang, J., Zhang, Y., Zhang, C., Wang, Y., Zhou, J., Whalley, L. K., Slater, E. J., Dyson, J. E., Xu, W., Cheng, P., Han, B., Wang, L., Yu, X., Wang, Y., Woodward-Massey, R., Lin, W., Zhao, W., Zeng, L., Ma, Z., Heard, D. E., Ye, C.: Validating HONO as an intermediate tracer of the external cycling of reaction nitrogen in the background atmosphere. Environ. Sci. Technol., 57, 13, 5474-5484, doi:10.1021/acs.est.2c06731, 2023.

[27] Xia, X., Zong, X., Cong, Z., Chen, H., Kang, S., and Wang, P.: Baseline continental aerosol over the central Tibetan plateau and a case study of aerosol transport from South Asia, Atmos. Environ., 45, 7370-7378, doi: 10.1016/j.atmosenv.2011.07.067, 2011.

[28] He, S., Wang, S., Zhang, S., Zhu, J., Sun, Z., Xue, R., Zhou, B.: Vertical distributions of atmospheric HONO and the corresponding OH radical production by photolysis at the suburb area of Shanghai, China. Sci. Total Environ., 858, 159703, doi:10.1016/j.scitotenv.2022.159703, 2023.